11-2021

Assessing Deep Convection Initiation in a Mountain-Valley System Using Unoccupied Aircraft System Observations

Alexander Erwin
University of Nebraska-Lin, alex.erwin@huskers.unl.edu

ASSESSING DEEP CONVECTION INITIATION IN A MOUNTAIN-VALLEY SYSTEM USING UNOCCUPIED AIRCRAFT SYSTEM OBSERVATIONS

by

Alexander J. Erwin

A THESIS

Presented to the Faculty of

The Graduate College at the University of Nebraska

In Partial Fulfillment of Requirements

For the Degree of Master of Science

Major: Earth and Atmospheric Sciences

Under the Supervision of Professor Adam L. Houston

Lincoln, Nebraska

September, 2021

ASSESSING DEEP CONVECTION INITIATION IN A MOUNTAIN-VALLEY SYSTEM USING UNOCCUPIED AIRCRAFT SYSTEM OBSERVATIONS

Alexander J. Erwin, M.S.

University of Nebraska, 2021

Advisor: Adam L. Houston

Forecasts of the timing and location of deep convection are inadequate, as are scientists' understanding of the dominant controlling mechanisms. The Lower Atmosphere Process Studies at Elevation, a Remotely-piloted Aircraft Team Experiment (LAPSE-RATE) field campaign, which took place in the San Luis Valley (SLV) of Colorado during July 2018, aimed to use in-situ observations to develop a deeper understanding of the processes relevant to deep convection initiation (DCI). The campaign resulted in a unique dataset, collected by a network of unoccupied aircraft systems (UAS) in a unique geographic setting, which can be used to examine the impact of terrain and land surface heterogeneity on DCI. During the first convection initiation-focused intensive operation period (IOP) of LAPSE-RATE, convection developed over the mountains first, produced an outflow boundary that moved into the SLV and subsequently played a role in DCI in the SLV. The objective of this research is to determine if mesoscale thermodynamic and kinematic 'hot spots' exist and if these correspond to the locations of DCI. This research highlights the value of dense networks of profiling UAS for sampling planetary boundary layer (PBL) features, including those relevant to the timing and location of DCI.

Acknowledgements

I would like to thank my advisor, Dr. Adam Houston, for the opportunity to conduct research with the Severe Storms Research Group at the University of Nebraska and continuing to support and guide my research as I took on a new job partway through the completion of this project. I would also like to thank my committee members, Dr. Clinton Rowe and Dr. Matthew Van Den Broeke, for their suggestions and feedback throughout this project.

I would also like to thank the more than 100 scientists and numerous institutions (including the University of Colorado-Boulder, University of Kentucky, University of Oklahoma, Oklahoma State University, Black Swift Technologies, and the National Severe Storms Laboratory) who were involved in the LAPSE-RATE field campaign. Without their efforts to collect and quality control the LAPSE-RATE data, this work would not have been possible. I would also like to thank the NSF CLOUD-MAP grant for funding this research.

I would like to thank the many friends I made at the University of Nebraska, who have kept me on track and helped motivate me at times when this work became daunting. And above all, I would like to thank my parents for their unwavering support and confidence in my abilities both during this project and over the course of my academic career.

TABLE OF CONTENTS

1. Introduction

Deep atmospheric convection is the transport of fluid along the gravitational force vector, owing to the release of thermal instability. Deep atmospheric convection often leads to the production of precipitation below the cloud base. It has a wide range of impacts, such as damaging severe weather, locally intense rainfall, and vertical mass transport, which affect a variety of industries including aviation, agriculture, and climate modeling (e.g., Hillaker and Waite 1985, Marshall 2002, Mecikalski et al. 2007, Zhu 2015). The identification criteria for deep convection initiation (DCI) varies, but numerous prior studies use the first occurrence of radar reflectivity values greater than 30-40 dBZ (e.g., Wilson and Schreiber 1986, Weckwerth 2000, Weckwerth et al. 2008, Frye and Mote 2010, Roberts et al. 2012, Weckwerth et al. 2014, Stelten and Gallus 2017, Trier et al. 2017). In addition to the aforementioned radar reflectivity thresholds, the areal extent of the radar echo or the production of cloud-to-ground lightning are sometimes used as identification criteria for DCI (e.g., Wilson and Roberts 2006, Sieglaff et al. 2011, Lock and Houston 2014, Soderholm et al. 2014, Houston et al. 2015, Steltan and Gallus 2017).

Despite its highly impactful nature, forecasts of the timing and location of DCI are inadequate. This inadequacy stems in large part from a significant deficiency in the spatiotemporal resolution of thermodynamic and kinematic observations in the lower troposphere, especially in the vertical (e.g., Weckwerth 2000, Cai et al. 2006, Wilson and Roberts 2006, Weckwerth et al. 2008, Roberts et al. 2012, Nugent and Smith 2014). Small variations in boundary layer temperature, $O(1\ \mathrm{K})$, and moisture, $O(1\ \mathrm{g\ kg^{-1}})$, have significant impacts on DCI potential (Crook 1996). The current atmospheric profiling

network uses radiosondes launched twice daily from 92 locations across the United States, which is an extremely sparse spatiotemporal resolution for effective use in DCI forecasting (*National Academy of Sciences* 2009). For example, a sounding launched less than 15 km from an ongoing thunderstorm during the Convection and Precipitation Electrification campaign (CaPE 1991) indicated that DCI was not likely; but by modifying the sounding with observations from a research aircraft that flew through the updraft branch of a horizontal convective roll, a more accurate representation of convective potential was obtained (Weckwerth 2000). The lack of observations impacts not only forecasting, but also scientists' ability to develop a deeper understanding of the processes that regulate DCI. Scientists understand that the maintenance of positive buoyancy through deep ascent, which defines deep convection, is controlled by complex interactions between buoyancy, lift, and dilution. There are several environmental parameters that can be used to assess these factors; however, there is no precise combination of parameter values that ensure DCI will occur, and the insufficient resolution of observations impacts the accuracy of the parameters (Lock and Houston 2014).

2. Background

Traditional parcel theory, which is frequently used to evaluate the potential for deep convection, is based on the assumption that rising motion is only a function of buoyancy. A parcel is lifted dry adiabatically, conserving potential temperature and mixing ratio, until becoming saturated at the lifting condensation level (LCL). Thereafter, the parcel is lifted pseudoadiabatically, conserving pseudoequivalent potential temperature. A pseudoadiabatic process is a moist adiabatic process for which the heat capacity of liquid water is neglected, that is, any liquid water is assumed to be lost from the parcel. As the parcel rises, the level of free convection (LFC) is the point at which it first becomes warmer than its environment and begins to release gravitational/thermal instability.

Two commonly used convective parameters that utilize parcel theory are convective available potential energy (CAPE) and convective inhibition (CIN). CAPE is a measure of positive buoyancy. Larger CAPE values suggest the updraft will be more vigorous if a parcel reaches its LFC. However, larger CAPE values may not imply that DCI will more readily occur. CIN is a measure of the negative buoyancy a parcel must overcome to reach its LFC. A smaller magnitude of CIN suggests less forced ascent is required to lift a parcel to the point at which it becomes buoyant; however, zero CIN does not imply DCI will occur (Houston and Niyogi 2007; Lock and Houston 2014). Additional convective parameters include Δz^* (Houston and Niyogi 2007), the minimum amount of lift required for any parcel from a particular vertical profile to reach its LFC, and the active cloud-bearing layer lapse rate (ACBLLR), the lapse rate of the layer from the LFC to 1.5 km above the LFC, both of which employ the LFC height, which is

determined using parcel theory. The ACBLLR is a proxy for the impact of dilution above cloud base, such that smaller ACBLLR values indicate increased deleterious effects from dilution and imply that DCI is less likely to occur (Houston and Niyogi 2007).

Traditional parcel theory neglects the perturbation vertical pressure gradient force, dilution, and hydrometeor loading, all of which modify parcel ascent. It also neglects freezing, which can increase buoyancy via latent heat release (Markowski 2007). These neglected processes play a significant role in DCI, such that even if the observations used to assess the environment are accurate, and there is sufficient lift for a parcel to reach its LFC, DCI is not guaranteed. For example, the rate of buoyancy reduction due to dilution above the LFC can outpace the buoyancy increase due to ascent. Thus, for DCI to occur, a parcel must reach a supercritical state where the increase in buoyancy due to ascent outpaces any deleterious effects (Houston and Niyogi 2007).

In a mountain-valley system, the elevated terrain is a preferred location for pristine DCI, that is, DCI that occurs in the absence of any ongoing convection in the vicinity. Valleys have substantially fewer pristine initiation points than any nearby elevated terrain (Banta and Barker Schaaf 1987). There are several mechanisms driven by elevated terrain, such as orographic lift, lee side convergence, wake effects, channeling, and secondary circulations associated with heating, which ultimately result in lift (Fig. 1) (Banta and Barker Schaaf 1987). This lift can provide a ‘triggering’ mechanism by lifting parcels to their LFC and can also result in environmental preconditioning through multiple successive thermals. Multiple successive thermals detrain moisture and cool the environment via ascent, which simultaneously reduces the impact of dilution and increases the buoyancy, thus making DCI more likely (e.g., Zhao and Austin 2005, Wu et

al. 2009, Kirshbaum 2011, Lock and Houston 2014, Panosetti et al. 2016). It is worth noting that this preconditioning effect over elevated terrain is highly dependent on the wind direction, such that even a weak cross-ridge wind may advect moisture away and reduce the preconditioning effect (Kirshbaum 2011, Weckwerth et al. 2014).

Low-level convergence zones, such as frontal boundaries, horizontal convective rolls, convective outflow boundaries, sea-breeze circulations, differential heating boundaries, and more, are also localized regions of ascent and favorable regions for DCI (Purdom 1982, Wilson and Schreiber 1986). A three-month study in eastern Colorado found that 79% of thunderstorms initiated near a low-level convergence zone (Wilson and Schreiber 1986). However, not all low-level convergence zones produce deep convection, and there is significant along-line variability in the thermodynamic and kinematic structure of a low-level convergence zone, making it challenging to identify if, when, and where DCI will occur (Wilson and Schreiber 1986, Cai et al. 2006).

One unique type of low-level convergence zone is a non-classical mesoscale circulation (NCMC), which develops in response to surface sensible heat flux gradients (Segal and Arritt 1992, McPherson et al. 2004). An NCMC is similar in structure to a sea-breeze circulation, but develops as a result of gradients in soil moisture, vegetation, snow cover, or cloud cover (Segal and Arritt 1992). In a sea breeze circulation, sensible heat flux differences of up to a few hundred watts per square meter result in surface temperature differences of up to several kelvins. The temperature differences induce a horizontal perturbation pressure gradient force that results in surface convergence over the region of larger sensible heat flux. This surface convergence generates a pressure excess, leading to an upward-directed vertical perturbation pressure gradient force and

rising motion. The opposite is true over the region of smaller sensible heat flux, such that there is surface divergence, a surface pressure deficit, a downward-directed perturbation pressure gradient force, and sinking motion. A circulation forms linking the two regions, such that there is surface flow from the smaller heat flux region to the larger heat flux region at the surface, and the opposite at some higher altitude. Modeling studies found that under idealized conditions, the strength of an NCMC can be similar to that of a sea breeze circulation (Segal and Arritt 1992). The strength of a vegetation-driven NCMC is impacted by the size and uniformity of both the vegetated and dry regions, as well as the quantity, type, and condition of the vegetation (Segal and Arritt 1992, McPherson et al. 2004). For an NCMC to develop, the thermally-driven perturbation pressure gradient force must be strong enough to counteract any ambient winds. In a mountain-valley system, upslope flow can distort the development of an NCMC (Segal and Arritt 1992). Nevertheless, the potential exists for an NCMC to provide sufficient lift to induce DCI (Pielke 2001, Frye and Mote 2010).

Regardless of the development or strength of an NCMC, lateral gradients in land-use impact the thermodynamic structure of the lower troposphere (Segal and Arritt 1992, McPherson et al. 2004, McPherson and Stensrud 2005). A winter wheat belt in Oklahoma produced statistically significant cool and moist surface anomalies during the winter growing months compared to the adjacent vegetation-free regions to both the west and the east (McPherson et al. 2004). During the summer months, the winter wheat belt, which was bare compared to the neighboring areas, exhibited warm and dry surface anomalies. A closer examination revealed that, depending on the ambient wind direction and location of station relative to the winter wheat belt, microscale anomalies of moisture

and temperature developed as a result of the land-use gradients (McPherson et al. 2004). While prior work has examined how land-use gradients impact thermodynamics at the surface and, in some cases, at some height level above the surface (Segal et al. 1989), it remains unclear how land-use gradients impact the thermodynamics throughout the entire layer. Given that small variations in planetary boundary layer (PBL) thermodynamics can significantly impact DCI potential, it is anticipated that land-use gradients can substantially impact DCI potential.

These geographic considerations make the San Luis Valley (SLV) of Colorado an ideal location to examine DCI in a mountain-valley system. The valley has an average elevation of 2336 m above mean sea level (MSL). It is surrounded by tall mountain ridges on all sides, such as the Sangre de Cristo Mountains (maximum elevation: 4374 m above MSL) to the east, the Culebra Range (4283 m above MSL) to the southeast, and the San Juan Mountains (4361 m above MSL) to the west. The SLV itself has substantial land-use gradients, with an irrigated region in the southwestern portion of the valley, and drier, non-irrigated land elsewhere (Fig. 2).

The Lower Atmosphere Process Studies at Elevation, a Remotely-piloted Aircraft Team Experiment (LAPSE-RATE) field campaign took place in the SLV 14-20 July 2018 (de Boer et al. 2020). LAPSE-RATE was a collaborative project that included participants from the University of Colorado-Boulder, University of Nebraska-Lincoln, Oklahoma State University, University of Oklahoma, University of Kentucky, Virginia Tech University, Kansas State University, National Center for Atmospheric Research, National Severe Storms Laboratory, Finnish Meteorological Institute, Black Swift Technologies, and Engenius Micro. The campaign utilized a variety of instruments,

including rotary-wing and fixed-wing unoccupied aircraft systems (UAS), mobile mesonets, radiosondes, Doppler wind lidar, and surface-based towers, to investigate a variety of atmospheric boundary layer phenomena, including DCI. An array of profiling UAS were deployed across the SLV to collect boundary layer thermodynamics of unprecedented four-dimensional resolution during four different intensive operation periods (IOP), two of which were focused on DCI. In total, there were 1287 UAS flights during LAPSE-RATE.

The goal of this study is to use the observations collected during LAPSE-RATE IOP1 to gain a deeper understanding of the atmospheric boundary layer processes relevant to DCI in a mountain-valley system, as well as the impact that land-use gradients have on these processes. It is hypothesized that:

1. One mechanism by which DCI occurs over the SLV is through pristine DCI over the mountain ridges, which produces an outflow boundary that propagates into the SLV and plays a vital role in DCI over the valley floor.
2. Land-use gradients in the SLV result in the development of thermodynamic and kinematic ‘hot spots’ that correspond to the actual location of DCI.

3. Methodology

The UAS instrumentation that was incorporated in this work are listed in Table 1, adapted from Barbieri et al. (2019). On 14 July 2018, the first day of LAPSE-RATE, a sensor intercomparison was conducted. Each UAS flew at the same altitude as the extendable, instrumented mast of the ground-based Mobile UAS Research Collaboratory (MURC). Barbieri et al. (2019) presented mean differences and standard deviations of the on-board measurements of each UAS platform.

Even with this intercomparison, some uncertainty remains as to how to best address potential biases in the data. With only one intercomparison flight completed per platform, if a sensor was not well-aspirated or shielded from solar radiation, the mean difference computed during the intercomparison may vary significantly from the biases experienced under other atmospheric conditions (e.g., direct sunlight versus cloudy). For the platforms with well-aspirated and shielded sensors, we are confident that applying a bias correction based on the mean difference found during the intercomparison is the best approach. For platforms that had sensors without sufficient aspiration or solar shielding, the data were subjectively monitored for any obvious errors, but no bias corrections were applied. Table 2 contains a list of the intercomparison mean differences and data corrections applied. For all platforms, only the observations collected during flight ascent were used because, unless careful consideration is given to sensor placement and aspiration, observations obtained during flight descent are prone to errors (Hemingway et al. 2017).

The University of Kentucky applied a bias correction to some of their UAS data based on their own intercomparison work. This bias correction was removed prior to any

adjustments made for this work, then a bias correction based on the LAPSE-RATE intercomparison was applied to the raw University of Kentucky UAS data. Therefore, for some University of Kentucky platforms, the applied correction listed in Table 2 may be different than the intercomparison mean difference. The net change to the raw University of Kentucky data was equal to and opposite of the intercomparison mean difference. The University of Oklahoma UAS platforms had three identical temperature and relative humidity sensors per platform. The intercomparison work for these sensors computed a mean difference for each sensor. The UAS data provided by the University of Oklahoma were the means of the three sensors, after each was individually bias-corrected by the University of Oklahoma. The net change applied by the University of Oklahoma was equal to and opposite of the intercomparison mean difference; therefore, it was not necessary for us to apply a bias-correction to their UAS data.

The surface-based instruments present during LAPSE-RATE include three Automated Surface Observing System (ASOS) or Automated Weather Observing System (AWOS) surface stations, located at Del Norte (KRCV), Saguache (K04V), and Alamosa (KALS) (Fig. 3), two University of Nebraska-Lincoln Combined Mesonet and Tracker vehicles (UNL CoMeTs), and a University of Kentucky tower (UKY Tower). The surface-based instrumentation is detailed in Table 3.

Both the UAS and surface-based instruments collected observations of temperature, relative humidity, and pressure. After data corrections were applied, the observations were used to calculate derived variables, such as potential temperature (θ in Kelvin), virtual potential temperature (θ_v in Kelvin), equivalent potential temperature (θ_e

in Kelvin), mixing ratio (q_v in g kg^{-1}), and dew point temperature (T_d in °C). The equations used to calculate these quantities are listed below:

$$\theta = T\left(\frac{10^5}{p}\right)^{R_d/C_{pd}}$$

$$\theta_v = \theta\left(1 + 0.61 q_v\right)$$

$$\theta_e = \left[\theta\left(\frac{T}{\theta}\right)^{\frac{R_d q_v}{C_{pd}}}\right]^{\left(\frac{3376}{T_{LCL}} - 2.54\right)\left(q_v + 0.81 q_v^2\right)}$$

$$q_v = 62.2\frac{e}{p}$$

$$T_d = \frac{-5420}{\ln\left(\frac{p \cdot q_v}{62.2 \cdot 2.53 \times 10^9}\right)}$$

where, for these calculations, T is the air temperature in Kelvin, p is pressure in pascals, e is the vapor pressure in pascals based on $e = 0.01 \cdot RH \cdot e_s$, e_s is the saturation vapor pressure in pascals based on $e_s = 6.112^{\left[17.67\left(T - 273.15\right)/\left(243.5 + \left(T - 273.15\right)\right)\right]}$ from Wexler (1976) and Bolton (1980), T_{LCL} is the temperature at the LCL in Kelvin based on $T_{LCL} = 55 + \frac{2840}{3.5\ln\left(T\right) - \ln\left(e\right) - 4.805}$ from Bolton (1980), R_d is the gas constant of dry air, C_{pd} is the specific heat of dry air at constant pressure, and RH is the relative humidity in percent.

The observed and derived variables from each flight were interpolated in the vertical. Interpolating removed high-frequency variation in the observed data, ensured

there were data at the same heights above ground level (AGL) for every flight, and lessened the impact of errors in on-board altitude calculations (Barton 2012). Interpolation relied on the Cressman method, which calculates the interpolated values via a weighted sum of observations that fall within a user-defined radius of influence (Cressman 1959). If an observation is within the radius of influence, its weight is determined according to

$$W = (R^2 - r^2)/(R^2 + r^2)$$

where R is the radius of influence, and r is the distance between the observation and the grid point. If the observation is outside the radius of influence (r > R), its weight is set to zero, such that it has no impact on the interpolated value.

For the vertical interpolation, five corrective passes were made, each with a progressively smaller radius of influence. For the first pass, the radius of influence was set to 20 meters. In the successive passes, the radius of influence was decreased to 18, 16, 14, and 12 meters. As the radius of influence tightens, the interpolated values become more representative of the observations. The average vertical data spacing varied by platform, but was typically less than 1 m and always less than 3 m. As a result of the high frequency of observations, the interpolated data points closely resemble the observations.

Each pass calculates a new value for each point by using weighted differences to calculate a correction factor and applying the correction factor to the value from the last pass. The value of the ith grid point at the end of the new pass, f_i^{m+1} , is calculated according to

$$f_i^{m+1} = f_i^m + \frac{\sum_{k=1}^{K}[w_{ik}^m * (O_k - f_i^m)]}{\sum_{k=1}^{K} w_{ik}^m}$$

where f_i^m is the value of the ith grid point during the mth iteration, w_{ik}^m is the weighting function between the ith grid point and the kth observation during the mth iteration, and O_k is the value of the kth observation. After calculating all passes, the values from each pass, m, are averaged at each point, i, to create the final interpolated value. The lowest and highest 20 m of each flight were truncated. Truncating removed biases that are induced by interpolating the tail of the profile. For example, the interpolated pressure at the top of the profile is biased higher because all points within the radius of influence are from below that level. Additionally, truncating the lowest 20 m removed observations at heights where there was not sufficient time for aspiration to remove heating of the platform body and instruments by insolation (possible even for shielded sensors).

The first LAPSE-RATE IOP occurred on 15 July. The synoptic-scale pattern was conducive for DCI owing to the presence of monsoonal flow increasing moisture at all levels. Weak 0-6 km wind shear (less than 30 knots) was anticipated; as such, slow-moving, non-severe thunderstorms were expected. The sampling strategy for IOP1 was for UAS to complete a vertical profile every 30 minutes between 0800 LST (1400 UTC) and 1400 LST (2000 UTC), and radiosonde launches every three hours between 0600 LST (1200 UTC) and 1500 LST (2100 UTC). Most of the UAS flew up to 500 m AGL. If possible, UAS flew to 1000 m AGL; however, some platforms had manufacturer-imposed limitations that prevented flights higher than 500 m AGL, despite having the necessary Federal Aviation Administration (FAA) clearance to fly above that altitude. Another limiting factor at some locations was the presence of a military training route, which, when active, limited UAS operations to below 125 m AGL. If a platform's battery life allowed, multiple profiles were completed during a single flight.

In addition to vertical profiles, a mobile mesonet completed transects across the SLV[1]. The goal of these transects was to continuously sample the evolution of the near-surface thermodynamics when moving from irrigated land to non-irrigated land, potentially sampling a non-classical mesoscale circulation, if one existed. The locations of instrumentation used during IOP1 are shown in Fig. 3.

To evaluate the impact of land-use differences on convective potential, we seek to determine if the thermodynamics of the lower PBL varied in both height and time across the SLV during the 15 July event. First, flights were divided into two groups based on regional land-use in the vicinity of their profiling location: irrigated or non-irrigated. The distinction between irrigated and non-irrigated land is based on LANDSAT-8 Normalized Difference Vegetation Index (NDVI) imagery from June 2018 (Fig. 4). It is evident from the NDVI imagery that even in the irrigated region of the SLV, the irrigation was sporadic, which added some ambiguity in determining whether a location should be classified as irrigated or non-irrigated. For this work, a profiling location was classified as non-irrigated if it was at least two kilometers away from any irrigated land. All of the profiling locations classified as irrigated were located on or immediately adjacent to at least one plot of irrigated land. However, many of the irrigated profiling locations were away from the core of the irrigated land, and the atmosphere sampled at these locations may exhibit a less robust thermodynamic response than what would theoretically be expected over the core of the irrigated land. Advection was not considered when classifying the profiling locations, as the complexities of doing so were beyond the scope of this work.

[1] UAS were supposed to accompany the mobile mesonet, but transects by the UAS were unsuccessful owing to technical difficulties.

Another characteristic of the profiling locations that should be noted is their altitude. Generally speaking, altitude changes across the SLV are muted compared to the surrounding mountainous terrain. Almost all of the sampling locations were located between 2300-2330 m above MSL, with the exception of OU Coptersonde 2-A, K04V, CU-BST S1, and KRCV (Fig. 3). These four instruments were located on the far western side of the SLV, where the altitude was between 2380-2410 m above MSL.

The IOP1 flight operations plan called for each profiling location to perform a flight at least every 30 minutes; however, the availability of flight data at each location was inconsistent. For this analysis, we focused on 1500, 1600, 1700, and 1800 UTC, times at which a majority of locations were able to complete successful profiles. Likewise, the height range analyzed was 2400-2800 m above MSL, a range with consistent data availability from a majority of platforms. For each period and thermodynamic variable, a two-sided t-test was performed at each height level. Heights relative to MSL were used so that the data being compared were from the same horizontal slice through the atmosphere, rather than from different altitudes. Hereafter, heights referenced in this text are in meters above MSL, unless otherwise noted. The null hypothesis of the t-test was that both regions had identical thermodynamic characteristics. A difference between the two regions was deemed statistically significant, and the null hypothesis rejected, if the *p*-value was less than 0.05. A rejection of the null hypothesis implies that a meaningful difference existed between the two regions.

To evaluate the possible impact of thermodynamic differences on DCI potential, radiosonde observations (which spanned the entire troposphere) were modified using the vertically interpolated UAS observations from flights between 1700 and 1830 UTC. Of

the two radiosonde launch locations (NSSL at Leach, CLAMPS at Moffat) (Fig. 3), both released a radiosonde at 1729 UTC during IOP1. Despite some of the UAS profiling sites being closer to the Leach Airport (Fig. 3), only the 1729 UTC Moffat radiosonde sounding (Fig. 5) was used, for consistency, so that any differences in the convective parameters would be attributable to low-level thermodynamic differences captured by the UAS.

The sounding was modified by inserting UAS temperature and dew point temperature observations and applying a smoothing procedure. The smoothing procedure employed a constant rate of change in temperature and dew point temperature from the highest UAS observations through the next 350 m of the radiosonde observations. This smoothing procedure was subjectively determined through trial and error to produce reasonable profiles without smoothing too deep of a layer.

Using the modified soundings, convective parameters including CAPE, CIN, and ACBLLR were calculated using the 100-mb mixed layer parcel. The 100-mb mixed layer parcel is a parcel with the mean mixing ratio and potential temperature of the lowest 100 hPa. CAPE and CIN were calculated using MetPy 0.12.1 (May et al. 2017), which adopts formulas from Wallace and Hobbs (1977). In these formulas, we replace temperature with virtual temperature following the virtual temperature correction outlined in Doswell and Rasmussen (1994), resulting in:

$$CAPE = -R_d \int_{LFC}^{EL} (T_{v.parcel} - T_{v.env}) d\ln(p)$$

$$CIN = -R_d \int_{SFC}^{LFC} (T_{v.parcel} - T_{v.env}) d\ln(p)$$

where R_d is the gas constant of dry air, EL is the pressure of the equilibrium level, LFC is the pressure of the level of free convection, SFC is the pressure at the surface or beginning of parcel path, $T_{v.parcel}$ is the virtual temperature of the parcel, and $T_{v.env}$ is the virtual temperature of the environment. Δz^* was calculated as the minimum distance between the LFC and initial height across all unmixed parcels for each profile.

A similar approach was taken to modify the 1729 UTC Moffat radiosonde sounding using only surface-based observations from the 1700-1830 UTC period. This was done to determine if a signal in DCI potential identified by the UAS-modified soundings was also detectable using only surface-modified soundings. For the UKY Tower and UNL CoMeTs, the surface observation was a 10-minute average centered on the desired observation time. If a UNL CoMeT was in motion, a 3-minute average centered on the desired time was used. When computing convective parameters for a surface-modified sounding, any signal in the mixed layer convective parameters would be muted, because modifying only the surface data point has a relatively small impact on the 100-mb mixed layer potential temperature and mixing ratio. Thus, convective parameters for the surface-modified sounding were calculated using the surface-based parcel.

The modified profiles and their associated convective parameters were sorted by region. A two-sided t-test was used to evaluate the null hypothesis that both regions had equal values of each convective parameter. Differences were deemed statistically significant, and the null hypothesis rejected, if the *p*-value was less than 0.05.

To detect DCI during IOP1, Weather Surveillance Radar-1988 Dopplar (WSR-88D) radar data was used. The SLV is situated between three WSR-88D radars, KABX (Alberqueque, NM), KGJX (Grand Junction, CO), and KPUX (Pueblo, CO).

KABX is located 264 km south-southwest of Alamosa (KALS, Fig. 3), KGJX is located 205 km northwest of Saguache (K04V, Fig. 3), and KPUX is located 148 km northeast of UNL CoMeT-2's location (Fig. 3). Given the long distances from these radars to the SLV and the potential for beam blockage by the mountainous terrain, it is reasonable to question the quality of radar coverage across the SLV. To calculate the center of the radar beam above MSL, we use the following equation from Rinehart (2010), which assumes a standard atmosphere:

$$H = \sqrt{R^2 + (\frac{4}{3}r_e + H_0)^2 + 2R(\frac{4}{3}r_e + H_0)\sin(\varphi)} - \frac{4}{3}r_e$$

where H is the height of the center of the radar beam above sea level in kilometers, H_0 is the height of the radar above sea level in kilometers, R is the distance from the radar in kilometers, φ is the elevation angle of the radar in degrees, and R_e is the radius of the earth, 6374 km. The elevation and tower height data for the three radars can be found in Table 4, while the estimated beam heights are provided in Table 5.

The 0.5° scan from both KABX and KGJX were blocked by the mountainous terrain between the radar and the SLV. It is clear from Table 5 that KPUX not only provided the best radar coverage, but that the other two radars provided little to no useful radar coverage of the SLV. Therefore, for our work, DCI was identified as the first occurrence of radar reflectivity values greater than 35 dBZ on any of the lowest four KPUX elevation angles (0.5°, 0.9°, 1.3°, and 1.8°).

DCI occurred first over the Sangre de Cristo Mountains at 1655 UTC (Fig. 6a). Over the next hour and a half, additional convective cells developed over the mountains, but no DCI occurred within the SLV (Fig. 6b). The first occurrence of DCI within the SLV occurred at 1845 UTC, over non-irrigated land about 30 km northeast of Alamosa

(Fig. 6c). DCI occurred again at 1917 UTC, 10 km west of Moffat, over non-irrigated land (Fig. 6d). Two additional cells initiated at 1933 UTC, one near Moffat and another 15 km northeast of Moffat (Fig. 6e). These cells were both over non-irrigated land as well. The cell that was the closest to Moffat strengthened to have radar reflectivity values greater than 50 dBZ by 1950 UTC (Fig. 6f). While we are not concerned with cell strength, it is included to show that regardless of whether the threshold for DCI is set at 35 or 40 dBZ, DCI clearly occurred over non-irrigated land. By 2010 UTC, the cells ongoing within the SLV began to weaken, and they dissipated by 2035 UTC (Fig. 6g). At 2126 UTC, DCI occurred over irrigated land (Fig. 6h), but never exceeded 40 dBZ and dissipated by 2157 UTC. DCI occurred again over non-irrigated land at 2214 UTC, to the northeast of Alamosa (Fig. 6i). This cell began weakening by 2236 UTC and dissipated by 2300 UTC. After 2300 UTC, there were no more occurrences of DCI.

4. Results

a. PBL Thermodynamics

To examine the evolution of the PBL through the day, time-height cross sections were made for each UAS site. These cross sections were created using a linear interpolation scheme that calculated a point every 5 m in the vertical and every 10 minutes in time. The temporal frequency of the UAS observations varied by platform, with most UAS collecting profiles 30 minutes to one hour apart, but some fixed-wing UAS collecting profiles as little as five minutes apart. The times at which a platform collected a profile are indicated on the time-height cross sections with a solid vertical blue line (Fig. 7). The evolution from stable nocturnal boundary layer to well-mixed boundary layer can be seen in time-height cross sections of potential temperature (Fig. 7), which transitions from increasing with height to being constant with height. The depth over which potential temperature is constant above the surface increases in time as boundary layer mixing deepens. There were three sites (OU Coptersonde 2-A, OU Coptersonde 2-B, UKY BLUECAT5-D) where flights to 3200 m were conducted with good temporal continuity through the observation period. The two non-irrigated region (NIrgR) sites (OU Coptersonde 2-A, 2-B) became well-mixed to the 3200 m level approximately one hour before the irrigated region (IrgR) site (UKY BLUECAT5-D), around 1730 and 1830 UTC, respectively (Fig. 7).

To quantify the potential impact of land-use differences on the thermodynamics of the lower atmosphere, we compared the UAS data from each region using a two-sided t-test with a 95% confidence interval. The test was performed at heights and times at which most sites collected data and applied to each of the following thermodynamic

variables: potential temperature, virtual potential temperature, temperature, mixing ratio, relative humidity, and equivalent potential temperature. The two-sided t-test was used to identify the heights and times at which the null hypothesis, which was that both regions had identical thermodynamic characteristics, could be rejected. If the null hypothesis was rejected ($p < 0.05$), the alternative hypothesis, which was that the two regions had different thermodynamic characteristics, was accepted. In analyzing the results of these tests, the mean value, difference in mean value, and statistical significance are all discussed.

i. Potential Temperature

Potential temperature exhibited a clear, consistent difference between the IrgR and NIrgR. Collectively, the mean potential temperature of the NIrgR was higher than the IrgR at all heights (2400-2800 m) and times (15, 16, 17, 18 UTC) and was consistently warmer by 1-2 K (Figs. 8a-8d). The difference in mean potential temperature decreased with height at 15 and 16 UTC, but stayed nearly constant with height at 17 and 18 UTC as the boundary layer became well-mixed. The potential temperature difference was statistically significant ($p < 0.05$) at almost all heights and times (Fig. 8e-8h) indicating that the NIrgR had higher heat content than the IrgR. The statistical significance became inconsistent above about 2725 m (approximately 400-500 m above ground level, depending on location) and was marginal ($p \sim 0.05$) in the lowest 20 m analyzed at 16 UTC (Fig. 8f).

There are occasional sharp increases or decreases in the mean value. These are not natural, but rather an artifact of the varying availability of UAS data. The right column of Figure 8 (Panels i-j) shows the heights at which data are available from each platform at a

given time. These allow for easy identification of when a spike in the mean data was the result of the addition or drop-out of a flight. Each of the thermodynamic figures mentioned hereafter includes a right column which shows the heights at which data is available from each platform (Figs. 8-11).

ii. Virtual Potential Temperature

Similar to potential temperature, the mean virtual potential temperature was also greater over the NIrgR at all heights and times, and the difference was generally between 1-2 K (Figs. 9a-9d). The heights and times at which the difference in virtual potential temperature was statistically significant were similar to the trends outlined for potential temperature. For brevity, these trends are not reiterated here, but can be seen in Figs. 9e-9h.

iii. Mixing Ratio

Vertical profiles of mean mixing ratio for both the NIrgR and IrgR decrease with height, even after becoming well-mixed (Figs. 10a-10d). Moreover, the IrgR mean mixing ratio often decreased more with height than the NIrgR mean mixing ratio. The NIrgR mean mixing ratio was less than the IrgR mean at most heights and times, with the exception of some levels above 2700 m. At 15 UTC, the IrgR mean was approximately 1 g kg^{-1} higher up to 2650 m, but the difference decreased to about 0.5 g kg^{-1} from 2650 to 2800 m (Fig. 10a). At 16 UTC, the IrgR mean was more than 1 g kg^{-1} higher than the NIrgR mean at the lowest levels (2400-2420 m), between 0.75-1 g kg^{-1} higher from 2420 to 2725 m, and decreased rapidly with height above 2725 m such that there was little difference above 2775 m (Fig. 10b). At 17 UTC, the IrgR mean was nearly 1.5 g kg^{-1} greater than the NIrgR mean at 2400 m. The difference between the means decreased

with height and was less than 0.25 g kg^{-1} above 2600 m. At a few points above 2700 m, the NIrgR mean was greater than the IrgR mean (Fig. 10c). At 18 UTC, the IrgR mean was greater at all heights, but the difference was less than 0.75 g kg^{-1} at all heights and often less than 0.5 g kg^{-1}, especially above 2600 m (Fig. 10d). At both 15 and 16 UTC, the difference in mixing ratio was statistically significant in the lowest 250 m analyzed (Fig. 10e, Fig. 10f). However, the significance decreased (*p*-value increased) as the day progressed, such that at 17 UTC, the difference was only statistically significant over the lowest 25 m analyzed (Fig. 10g); and by 18 UTC, there was not a statistically significant difference in moisture content between the two regions (Fig. 10h).

iv. Equivalent Potential Temperature

Unlike the other variables discussed to this point, the sign of the difference in mean equivalent potential temperature between the two regions changed over time. At 15 UTC, the IrgR mean equivalent potential temperature was 0.75-1 K greater between 2400-2650 m, but the difference decreased at higher heights (Fig. 11a). At 16 UTC, the IrgR and NIrgR profiles had similar mean values of equivalent potential temperature (Fig. 11b). At 17 UTC, the NIrgR mean was between 347.5-348.5 K, while the IrgR mean was nearly 1.5 K greater near the surface, but the IrgR mean decreased rapidly with height such that between 2475-2600 m, the NIrgR mean was approximately 1 K greater and 2 K greater above 2600 m (Fig. 11c). At 18 UTC, the IrgR mean was 0.5 K greater near the surface, the means were similar between 2410-2450 m, and above 2640 m the NIrgR mean was about 0.5-1 K greater than the IrgR mean (Fig. 11d). The differences in equivalent potential temperature were not significant at any height or

time (Figs. 11e-11h). For this variable, the null hypothesis, which was the two regions had the same mean equivalent potential temperature, could not be rejected.

b. Convective Parameters

To examine the extent to which these low-level thermodynamic differences impacted DCI potential, convective variables (CAPE, CIN, ACBLLR, Δz^*, LCL pressure and height, LFC pressure and height) were obtained by modifying the 1729 UTC Moffat sounding with UAS or surface observations collected between 1700-1830 UTC. A two-sided t-test with a 95% confidence interval was used to compare convective parameters, and test the alternative hypothesis that the convective parameters of the two regions were different.

i. UAS-modified Soundings

From 1700-1830 UTC, there were 15 UAS profiles from NIrgR locations and 13 from IrgR locations. For the UAS-modified soundings, the 100-mb mixed layer parcel was used to calculate convective parameters. The unmodified 1729 UTC Moffat sounding had 281 J kg^{-1} of mixed layer CAPE (MLCAPE) and -54 J kg^{-1} of mixed layer CIN (MLCIN) (Table 6). The NIrgR had higher mean MLCAPE (365 J kg^{-1}), or greater instability, than the IrgR (275 J kg^{-1}), and less negative MLCIN (-29 J kg^{-1} to -59 J kg^{-1}), or less inhibition. The difference in MLCAPE between the two regions was not statistically significant ($p = 0.143$), but the difference in MLCIN was ($p = 0.0017$). Relative to the unmodified 1729 UTC Moffat sounding, the mean MLCAPE and MLCIN of the NIrgR was more favorable for DCI, while the IrgR means were similar or slightly less favorable. There was little difference in ACBLLR between the two regions ($p = 0.46$), and Δz^* was identical for all profiles, since the minimum distance from a

parcel's starting height to its LFC occurred for a parcel originating above the level where UAS data were available. The NIrgR had lower mean LCL pressure than the IrgR region, but a higher LFC pressure. The difference in LCL pressure was statistically significant ($p = 0.0126$) while the difference in LFC pressure was not ($p = 0.386$). An investigation of LCL and LFC heights (AGL) was included to account for surface altitude differences across the SLV, which are not captured in the pressure-based calculation. The height-based calculation revealed a similar trend as the pressure-based calculation. The NIrgR had higher LCL heights, which is logical given that the NIrgR was often warmer and drier than the IrgR, and lower LFC heights. A lower LFC height is indicative of less lift required for a parcel to rise buoyantly. The difference in LCL height was statistically significant ($p = 0.04925$), while the difference in LFC height was not ($p = 0.11704$). Collectively, these convective parameters imply that, despite the IrgR having higher low-level moisture content, the NIrgR was more favorable for DCI.

ii. Surface-modified Soundings

From 1700-1830 UTC, there were 24 surface observations from NIrgR locations and 13 from IrgR locations. For these modified soundings, the surface-based parcel was used to calculate convective parameters, rather than the 100-mb mixed layer parcel. The unmodified 1729 UTC sounding had 629 J kg^{-1} of surface-based CAPE (SBCAPE) and 0 J kg^{-1} of surface-based CIN (SBCIN; Table 7). The surface-modified soundings showed that the NIrgR had lower mean SBCAPE (1052 J kg^{-1}) and more negative mean SBCIN (-6 J kg^{-1}) than the IrgR (1194 J kg^{-1} SBCAPE, -2 J kg^{-1} SBCIN). However, the differences in SBCAPE and SBCIN were not statistically significant. The SBCIN was zero for almost all surface-modified soundings. Only three NIrgR surface-modified

soundings (out of 24) and one IrgR (out of 13) had any SBCIN; therefore, the mean values were driven largely by those few soundings. The IrgR had higher LCL and LFC pressures (lower LCL and LFC heights) than the NIrgR at a statistically significant level. In summary, unlike for UAS-modified soundings, the convective parameters from surface-modified soundings would imply that the IrgR is more favorable for DCI than the NIrgR.

c. Low-Level Convergence Zones

Before drawing conclusions as to how land-use differences impacted DCI during IOP1, other environmental influences must also be considered. Archived surface maps from the National Oceanic and Atmospheric Administration's Weather Prediction Center (WPC) indicated that a cold front extended from an occluded surface low pressure in the Canadian Prairie Province southeastward across the northern Great Plains and into central Colorado, transitioning into a stationary front oriented east-west across Colorado (Fig. 12). In the WPC analysis, this frontal boundary remained positioned across central Colorado through much of the day on 15 July before pushing into southern Colorado by 00 UTC on 16 July. Due to relatively sparse surface observations and varying topographic influences in western and central Colorado, it is difficult to evaluate the evolution of the frontal boundary's position. However, in eastern and northeastern Colorado, 17 UTC surface observations showed flow ranging from northerly to northeasterly at locations north of the Arkansas River, with temperatures ranging from the mid-60s to low-80s °F (Fig. 13). Near and south of the Arkansas River, flow was just north of easterly with temperatures in the mid-80s to low-90s °F. Based on these observations and the east-west orientation of the frontal boundary on the WPC surface

analysis map, the frontal boundary was likely near the northern fringes of the SLV, approximately 50 km north of the Saguache Airport (K04V) (Fig. 3), at 17 UTC.

UNL CoMeT-2 and the UKY Tower took continuous surface observations at fixed locations within the SLV (Fig. 3). Between 15 and 18 UTC at UNL CoMeT-2's location, winds were generally northwesterly and light (less than 4 m s^{-1}). Temperatures warmed from 20 °C to 26 °C, with frequent fluctuations of 2-3 °C. Dew point temperature varied from 9 to 12 °C, trending towards the drier end of that range towards 18 UTC (Fig. 14). At 1813 UTC, winds shifted from northwesterly to east-southeasterly, but the temperature, dew point temperature, and wind speed remained in line with the trends established over the previous few hours. The winds maintained an easterly and/or southerly component, and the wind speed increased after 1830 UTC, varying between 6 to 12 m s^{-1}. Despite the wind shift and increase, there was still no noticeable change in the temperature and dew point temperature trends until 1838 UTC, when dew point temperature, which was near 10 °C, decreased rapidly to less than 6 °C by 1845 UTC. There was no obvious change in the temperature over this same time frame. The first occurrence of DCI within the SLV was at 1845 UTC (Fig. 6c). Three additional cells initiated, all over non-irrigated land, within the next 50 minutes (1845-1935 UTC). The dew point temperature continued to decrease gradually through 21 UTC, reaching a minimum of around 3 °C.

The decrease in dew point temperature and lack of temperature change observed at UNL CoMeT-2 is not consistent with the passage of an outflow boundary. Instead, it is hypothesized that this feature is the synoptic front (Fig. 12) progressing southward. The observed easterly wind is consistent with what would be expected on the north side of an

east-west-oriented stationary front. The easterly winds mean that wind was flowing downslope from the mountains into the SLV, which was not the case prior to frontal passage, and this downslope flow may explain why the air was considerably drier following the frontal passage. Around 21 UTC, an outflow boundary associated with convection over the NIrgR crossed UNL CoMeT-2's location, resulting in winds shifting to north-northwesterly with wind speeds of 6-10 m s^{-1}, and dew point temperature increasing sharply to about 8 °C.

The frontal passage observed at UNL CoMeT-2 was less apparent in the UKY Tower observations. Through 1945 UTC, the winds at the UKY Tower were variable with speeds below 5 m s^{-1} and dew point temperatures at or above 9 °C (Fig. 15). At 1945 UTC, about one hour after the frontal passage was noted at UNL CoMeT-2, winds at the UKY Tower shifted to easterly and increased to near 5 m s^{-1}, with gusts to 7.5 m s^{-1}. These gusts are lighter than what was observed following the easterly wind shift at CoMeT-2. Following the wind shift, there was no clear upward or downward trend in dew point temperatures, but they did exhibit larger variance than what had been observed prior to 1945 UTC. Based on these observations, it is hypothesized that the post-frontal air mass was spreading southwestward in time, becoming more diffuse as it did, such that the wind speeds behind the front weakened and the changes in dew point temperature were less obvious. Around 2045 UTC, an outflow boundary passed the UKY Tower with an associated wind shift to northerly, increase in wind speeds, increase in dew point temperature, and decrease in temperature (Fig. 16). The passage of this outflow boundary occurred 10 minutes after the cells over non-irrigated land dissipated (Fig. 6g) and 40 minutes before DCI occurred over irrigated land (Fig. 6h).

5. Discussion

a. Land-Use Differences

During IOP1, UAS profiles, collected hourly at ten fixed locations across the SLV, revealed that statistically significant differences in boundary layer thermodynamics such as potential temperature, water vapor mixing ratio, and virtual potential temperature, developed between the non-irrigated and irrigated regions and that the differences often extended several hundred meters in the vertical. These thermodynamic differences are consistent with the theoretical differences in sensible heat flux that should be expected between non-irrigated and irrigated surfaces. Specifically, over irrigated land there is lower sensible heat flux as a portion of the incoming energy is used to evaporate soil moisture (Frye and Mote 2010). This would suggest that over non-irrigated land, there will be higher heat content and lower moisture content, and that is indeed what was seen in the UAS observations from IOP1. This trend is consistent with those identified in prior observational studies (Segal and Arritt 1992, McPherson et al. 2004a, McPherson et al. 2004b, Frye and Mote 2010). However, much of the existing literature related to the impacts of land-use differences on the lower atmosphere was confined to using surface-based observations, leaving questions as to how high above the surface these thermodynamic differences extend and what impact they can have on the structure of the PBL (McPherson et al. 2004b).

Our work expands upon the existing literature by providing observational evidence of the extent to which land-use difference-induced thermodynamic dissimilarities exist above the surface. Soil Moisture Active Passive (SMAP) data for July 2018 from the National Snow and Ice Data Center reveal that there was indeed

higher soil moisture (generally greater than 0.3 cm^3 cm^{-3}) over irrigated land compared to non-irrigated land (often less than 0.1 cm^3 cm^{-3}) (Fig. 17). During IOP1, potential temperature was 1-2 K warmer over the NIrgR and the difference was statistically significant at most heights and times analyzed, indicating that the NIrgR had higher heat content that the IrgR. The IrgR had higher moisture content than the NIrgR at most heights and times analyzed, but the difference lessened to a point that it was not statistically significant at higher heights or later in the morning. This suggests that while differences in moisture content do develop, they may not be as robust as the differences in heat content. However, this result may be specific to an arid climate, such as the SLV. Additional work is needed to investigate the extent to which land-use differences impact low-level atmospheric moisture content. Ideally, this additional work would be conducted in various climate regions, including climate regions with higher soil moisture content than the SLV.

Numerical modeling studies have shown that land-use differences can impact the structure of the PBL and result in a shallower PBL over irrigated land or, in some cases, a non-classical mesoscale circulation (Segal et al. 1989, Segal and Arritt 1992, McPherson et al. 2004b). However, there have been limited observations of these features. UAS observations from IOP1 revealed a shallower PBL over irrigated land through at least 1730 UTC, confirming the capability of land-use differences to alter the PBL structure. Reduced mixing within the shallower PBL can result in higher moisture content in the PBL over irrigated land, which is what was observed during IOP1, at least in the earlier hours analyzed (15, 16 UTC).

While clear trends were established in the aforementioned thermodynamic variables, one variable that did not show a clear trend and did not have any statistically significant differences between the two regions was equivalent potential temperature. Equivalent potential temperature takes into account both potential temperature and mixing ratio, such that, for a given value of equivalent potential temperature, if one of these variables is lowered, an increase in the other can compensate and produce a similar value of equivalent potential temperature. This is likely the reason we see similar equivalent potential temperature values between the NIrgR and IrgR, with the increase (decrease) in potential temperature over the NIrgR (IrgR) counteracted by the decrease (increase) in mixing ratio.

b. Deep Convection Initiation

Larger values of equivalent potential temperature indicate greater potential instability, and the lack of a clear difference between the two regions could lead one to believe that land-use differences did not have much of an influence on DCI potential during IOP1. However, despite the similar equivalent potential temperature values, traditional DCI metrics calculated from UAS-modified soundings collected between 1700-1830 UTC suggested that the NIrgR was more favorable for DCI than the IrgR. The NIrgR had higher mean MLCAPE (greater instability) and less negative MLCIN (less inhibition), although the difference in MLCAPE was not statistically significant. This result suggests that the increase in heat content over the NIrgR, owing to greater sensible heat flux, was enough to create a more favorable instability profile despite lower moisture than the IrgR.

The finding that PBL thermodynamics were more favorable for DCI over the NIrgR is in contrast to Segal et al. (1989), which noted that DCI was more favorable over irrigated land owing to higher mixing ratio in the PBL. However, the Segal et al. (1989) study took place in northeast Colorado, not the SLV, and differences in the proportion of irrigated land or magnitude of the irrigation between the two studies may be the cause of this apparent discrepancy. It is worth noting that when the 1729 UTC Moffat sounding was modified using only surface observations, the surface-based DCI parameters suggested the IrgR was more favorable. Whether surface-based or mixed layer parameters have more merit is beyond the scope of this work, but the DCI evolution seen during IOP1 suggests the UAS-modified soundings better captured the true DCI potential than the surface-modified soundings.

The UAS-modified soundings suggest that DCI was more favorable over the NIrgR and that is ultimately where DCI first developed in the SLV during IOP1. Therefore, one could draw the conclusion that land-use differences were sufficient to support DCI over the NIrgR and limit DCI over the IrgR; however, we must caution against jumping to this conclusion. DCI is a complex process that occurs on a variety of scales and depends on a variety of factors, many of which are still not fully understood, making it unfeasible to attribute its occurrence (or lack thereof) solely to the impacts from land-use differences.

While the UAS observations collected during LAPSE-RATE provided valuable insights as to how land-use differences impacted thermodynamics and contributed to enhanced or reduced DCI potential, they did not collect information regarding the strength of lift along the low-level convergence zones. The role of lift, which is not

captured by traditional DCI metrics, was noted by Lock and Houston (2014) as the most influential of all the DCI factors (lift, buoyancy, inhibition, and dilution). During IOP1, all instances of DCI over the NIrgR occurred within an hour of a low-level convergence zone, likely the synoptic front, passing UNL CoMeT-2's location, and all instances of DCI over the IrgR occurred within an hour of an outflow boundary passing the UKY Tower's location. This evolution in which low-level convergence zones play a role in DCI has been widely noted in prior research (Purdom 1982, Wilson and Schreiber 1986, Banta and Barker Schaaf 1987, Weckwerth and Parsons 2006, Roberts et al. 2012). While we are confident that low-level convergence zones played a key role in the DCI process within the SLV during IOP1, the full impact cannot be quantified from the available observations. Additionally, our ability to track the location of the low-level convergence zones was reduced due to a lack of low-level WSR-88D coverage, further limiting our ability to link the occurrence of DCI to the low-level convergence zones. This is a known issue in mountainous areas owing to long distances from radars and potential beam blockage by terrain (Weckwerth et al. 2014). Even if we had been able to track the low-level convergence zones, uncertainty as to their role in DCI would remain as there are a number of factors, such as the orientation of storm-steering winds relative to the convergence zone (Roberts and Rutledge 2003, Kirshbaum 2011) and the thermodynamics on both sides of the boundary (Weckwerth and Parsons 2006), that we have not begun to consider here.

Ultimately, our research is another example that an increase in PBL observations can improve our assessment of DCI potential (e.g., Crook 1996, Weckwerth 2000, Weckwerth 2004, Markowski et al. 2006). However, the increase in observations has not

yet led to a clearer understanding of the processes regulating DCI, owing to the use of traditional DCI parameters based on 1-D profiles that do not capture all of the relevant processes. There is a role of both thermodynamics and kinematics in the DCI process, but quantifying the impact of each remains elusive. For example, in IOP1, it is not clear whether the DCI was more robust over the NIrgR because the land-use differences resulted in more favorable thermodynamics, thus requiring less lift for parcels to reach their LFC, or if lift along the low-level convergence zone was stronger over the NIrgR due to proximity to the source, resulting in sufficient (insufficient) lift over the NIrgR (IrgR) to bring parcels to their LFC. Both factors likely played a role in the occurrence, timing, and location of DCI during IOP1.

c. UAS and Future Work

This work joins a quickly expanding list of studies that demonstrate the usefulness of UAS for collecting atmospheric observations within the PBL (Palomaki et al. 2017, Koch et al. 2018, Lee et al. 2018, Leuenberger et al. 2020, Kral et al. 2021, van den Heever et al. 2021). Data were collected by a variety of UAS platforms, sensors, and sensor housings, so it would be reasonable for one to question the consistency of the data. When utilizing the UAS data, we took every possible measure to ensure that only quality data were incorporated into this work and that the data were quality controlled in a consistent manner based on the intercomparison work of Barbieri et al. (2019). There were a number of platforms with sensors that were not properly shielded or aspirated, and the lack of proper shielding and/or aspiration resulted in obvious biases in the data collected from these platforms that could not be removed. As a result, there were several UAS sampling locations from IOP1 that were not included in this work. The additional

data collected at these locations, had it been reliable, would have been valuable to our research. Our work is in agreement with the existing literature regarding the use of UAS data for data collection in atmospheric sciences, which suggests that UAS are a powerful tool for collecting meteorological observations, so long as the sensors are properly shielded and aspirated to yield reliable data (Greene et al. 2018, Jacob et al. 2018, Barbieri et al. 2019, Greene et al. 2019, Islam et al. 2019).

Another logistical recommendation from our work is to adhere to a consistent flight plan. While the original IOP1 flight plan was UAS profiles every 30 minutes, battery power, crew breaks, and gusty winds limited how often flights were conducted, with battery power being the largest constraint. One profile may require most or all of a battery pack's power, but fully charging a battery can take several times longer than the duration of a flight. So despite having multiple battery packs and the capability to charge batteries while conducting flights, some crews still missed their scheduled flight times due to battery limitations. Due to the inconsistent flight availability, there were a number of analysis methods that we hoped to incorporate into this research, including a four-dimensional objective analysis of the thermodynamic variables and vertical cross sections, which had to be abandoned. These power issues can be remedied by investing in additional batteries or designing the flight plan such that there is a greater temporal spacing between flights. Unfortunately, both of these solutions come at a cost, either literally or scientifically.

Additional work that could be done using the LAPSE-RATE dataset include an investigation of the other IOPs to determine whether similar PBL thermodynamic signatures were detected on other days. The other IOPs utilized different flight plans,

however, which may make it difficult to compare the data to IOP1. Future land-use studies could aim to conduct similar UAS sampling in areas with more coherent land-use regions and weaker ambient pressure gradients to deepen our understanding of how high above ground level these thermodynamic differences extend before weakening, and to try to obtain observations of an NCMC. As noted earlier in this section, in any such work it would be prudent to collect soil moisture and/or sensible heat flux observations at each UAS sampling location.

Another idea for future research would be the deployment of a targeted 3-D mesonet. The way in which UAS were utilized to create a network of UAS profiles across the SLV during IOP1 mirrors the 3-D mesonet concept proposed by Chilson et al. (2019), and our work showed that such a sampling method provides meaningful data on the thermodynamic variability of the PBL. While the 3-D mesonet proposed by Chilson et al. 2019 is a fixed feature, one can envision a future field project that deploys a 3-D mesonet to collect targeted observations of features of interest. One such feature could be a low-level convergence boundary. If utilized in concert with mobile radars, we may start to obtain a clearer picture of both the thermodynamic and kinematic structure on both sides of the low-level convergence zone and gain a deeper understanding of the role that both factors play in determining the ‘hot spots’ where DCI actually occurs.

6. Conclusions

On 15 July 2018, UAS collected vertical profiles at fixed locations across the SLV during IOP1 of the LAPSE-RATE field campaign. The goal was to assess the impact of land-use differences on the thermodynamics of the PBL and explore the processes regulating DCI in a mountain-valley system.

The UAS observations revealed that the NIrgR had higher heat content and lower moisture content than the IrgR and that the differences often extended several hundred meters above the surface. These thermodynamic differences resulted in traditional DCI metrics, calculated from UAS-modified soundings, implying that the NIrgR was more favorable for DCI. DCI occurred first over the NIrgR, and all instances of DCI within the SLV occurred within an hour of the passage of a low-level convergence zone. As prior studies have shown, the low-level convergence zones almost certainly played a key role in the DCI process during IOP1. The observations collected during IOP1 are not sufficient to attribute the occurrence of DCI directly to the impacts of land-use differences. Our current DCI metrics continue to be wholly insufficient for assessing DCI potential or the processes that regulate it, and one such area where additional observations are needed is in the vicinity of low-level convergence zones.

Future research could investigate the other LAPSE-RATE IOPs for similar signals in PBL thermodynamics. UAS continue to show utility in collecting higher spatiotemporal resolution observations of the PBL, but the sensors must be properly shielded and aspirated. Future UAS projects could utilize a similar UAS flight plan to obtain additional data related to the impacts of land-use differences, NCMC

development, low-level convergence zone impacts on DCI, or other mesoscale features of interest within the PBL.

7. References

Banta, R. M., and C. Barker Schaaf, 1987: Thunderstorm genesis zones in the Colorado Rocky Mountains as determined by traceback of geosynchronous satellite images. *Mon. Wea. Rev.*, **115**, 463-476.

Barbieri, L., and Coauthors, 2019: Intercomparison of small unmanned aircraft system (sUAS) measurements for atmospheric science during LAPSE-RATE campaign. *Sensors*, **19**, 2179.

Barton, J. D., 2012: Fundamentals of small unmanned aircraft flight. *John Hopkins APL Technical Digest*, **31**, 132-149.

Bolton, D., 1980: The computation of equivalent potential temperature. *Mon. Wea. Rev.*, **108**, 1046-1053.

Cai, H., W. Lee, T. M. Weckwerth, C. Flamant, and H. V. Murphey, 2006: Observations of the 11 June dryline during IHOP_2002 – A null case for convection initiation. *Mon. Wea. Rev.*, **134**, 336-354.

Chilson, P. B., and Coauthors, 2019: Moving towards a network of autonomous UAS atmospheric profiling stations for observations in the Earth's lower atmosphere: The 3D mesonet concept. *Sensors*, **19**, 2720.

Cressman, G. P., 1959: An operational objective analysis system. *Mon. Wea. Rev.*, **87**, 367-374.

Crook, A., 1996: Sensitivity of moist convection forced by boundary layer processes to low-level thermodynamic fields. *Mon. Wea. Rev.*, **124**, 1767-1785.

de Boer, G., and Coauthors, 2020: Development of community, capabilities, and understanding through unmanned aircraft-based atmospheric research – The LAPSE-RATE field campaign. *Bull. Amer. Meteor. Soc.*, **101**, 684-699.

Doswell, C. A., and E. N. Rasmussen, 1994: The effect of neglecting the virtual temperature correction on CAPE calculations. *Wea. Forecasting*, **9**, 625-629.

Frye, J. D., and T. L. Mote, 2010: Convection initiation along soil moisture boundaries in the Southern Great Plains. *Mon. Wea. Rev.*, **138**, 1140-1151.

Greene, B. R., A. R. Segales, S. Waugh, S. Duthoit, and P. B. Chilson, 2018: Considerations for temperature sensor placement on rotary-wing unmanned aircraft systems. *Atmos. Meas. Tech.*, **11**, 5519-5530.

Greene, B. R., A. R. Segales, T. M. Bell, E. A. Pillar-Little, and P. B. Chilson, 2019: Environmental and sensor integration influences on temperature measurements by rotary-wing unmanned aircraft systems. *Sensors*, **19**, 1470.

Hanft, W., and A. L. Houston, 2018: An observational and modeling study of mesoscale air masses with high theta-e. *Mon. Wea. Rev.*, **146**, 2503-2524.

Hemingway, B. L., A. E. Frazier, B. R. Elbing, and J. D. Jacob, 2017: Vertical sampling scales for atmospheric boundary layer measurements from small unmanned aircraft systems (sUAS). *Atmosphere*, **8**, 176.

Hillaker, H. J., and P. J. Waite, 1985: Crop-hail damage in Midwest Corn Belt. *J. Appl. Meteor. Climatol.*, **24**, 3-15.

Wallace, J. M., and P. V. Hobbs, 1977: *Atmospheric science: an introductory survey.* Academic Press, 350 pp.

Houston, A. L., and D. Niyogi, 2007: The sensitivity of convection initiation to the lapse rate of the active cloud-bearing layer. *Mon. Wea. Rev.*, **135**, 3013-3032.

Houston, A. L, N. A. Lock, J. Lahowetz, B. L. Barjenbruch, G. Limpert, and C. Oppermann, 2015: Thunderstorm observation by radar (ThOR): an algorithm to develop a climatology of thunderstorms. *J. Atmos. Oceanic Technol.*, **32**, 961-981.

Islam, A., A. L. Houston, A. Shankar, and C. Detweiler, 2019: Design and evaluation of sensor housing for boundary layer profiling using multirotors. *Sensors*, **19**, 2481.

Jacob, J. D., P. B. Chilson, A. L. Houston, and S. Weaver Smith, 2018: Considerations for atmospheric measurements with small unmanned aircraft systems. *Atmosphere*, **2018**, *9*, 252.

Kirshbaum, D. J., 2011: Cloud-resolving simulations of deep convection over a heated mountain. *J. Atmos. Sci.*, **68**, 361-378.

Koch, S. E., M. Fengler, P. B. Chilson, K. L. Elmore, B. Argrow, D. L. Andra Jr., and T. Lindley, 2018: On the use of unmanned aircraft for sampling mesoscale phenomena in the preconvective boundary layer. *J. Atmos. Oceanic. Technol.*, **35**, 2265-2288.

Kral S. T., and Coauthors, 2021: The innovative strategies for observations in the arctic atmospheric boundary layer project (ISOBAR): Unique finescale observations under stable and very stable conditions. *Bull. Amer. Meteor. Soc.*, **102**, 218-243.

Lean, H. W., N. M. Roberts, P. A Clark, and C. Morcrette, 2009: The surprising role of orography in the initiation of an isolated thunderstorm in Southern England. *Mon. Wea. Rev.*, **137**, 3026-3046.

Lee T. R., M. Buban, E. Dumas, and C. B. Baker, 2018: On the use of rotary-wing aircraft to sample near-surface thermodynamic fields: results from recent field campaigns. *Sensors*, **19**, 10.

Leuenberger D., A. Haefele, N. Omanovic, M. Fengler, G. Martucci, B. Calpini, O. Fuhrer, and A. Rossa, 2020: Improving high-impact numerical weather prediction with lidar and drone observations. *Bull. Amer. Meteor. Soc.,* **101**, 1036-1051.

Lock, N. A., and A. L. Houston, 2014: Empirical examination of the factors regulating thunderstorm initiation. *Mon. Wea. Rev.,* **142**, 240-258.

Madole, R. F., J.H. Romig, J.N. Aleinikoff, D.P. VanSistine, and E.Y. Yacob, 2008: On the origin and age of the Great Sand Dunes, Colorado. *Geomorphology*, **99**, 99-119.

Markowski, P., 2007: The concept of buoyancy and its application to deep moist convection, *Atmospheric Convection: Research and Operational Forecasting Aspects*, Giaiotti D.B., Steinacker R., Stel F. (eds), CISM International Centre for Mechanical Sciences, volume 475, Springer, Vienna, 7-15.

Marshall, T. P., 2002: Tornado damage survey at Moore, Oklahoma. *Wea. Forecasting*, **17**, 582-598.

May, R. M., Arms, S. C., Marsh, P., Bruning, E., and Leeman, J. R., 2017: MetPy: A Python package for meteorological data. Unidata, https://github.com/Unidata/MetPy.

McPherson, R. A., and D. J. Stensrud, 2005: Influences of a winter wheat belt on the evolution of the boundary layer. *Mon. Wea. Rev.,* **133**, 2178-2199.

McPherson, R. A., D. J. Stensrud, and K. C. Crawford, 2004: The impact of Oklahoma's winter wheat belt on the mesoscale environment. *Mon. Wea. Rev.,* **132**, 405-421.

Mecikalski, J. R. and Coauthors, 2007: Aviation applications for satellite-based observations of cloud properties, convection initiation, in-flight icing, turbulence, and volcanic ash. *Bull. Amer. Meteor. Soc.*, **88**, 1589-1607.

National Research Council, 2009. *Observing Weather and Climate from the Ground Up: A Nationwide Network of Networks.* Washington, DC: The National Academies Press, 250 pp.

Nugent, A. D., and R. B. Smith, 2014: Initiating moist convection in an inhomogeneous layer by uniform ascent. *J. Atmos. Sci.,* **71**, 4597-4610.

Palomki, R. T., N. T. Rose, M. van den Bossche, T. J. Sherman, and S. F. J. De Wekker, 2017: Wind estimation in the lower atmosphere using multirotor aircraft. *J. Atmos. Oceanic. Technol.,* **34**, 1183-1191.

Panosetti, D., S. Böing, L. Schlemmer, and J. Schmidli, 2016: Idealized large-eddy and convection-resolving simulations of moist convection over mountainous terrain. *J. Atmos. Sci.,* **73**, 4021-4041.

Pielke, R. A., 2001: Influence of the spatial distribution of vegetation and soils on the prediction of cumulus convective rainfall. *Rev. Geophys.,* **39**, 151-177.

Purdom, J. F. W., 1982: Subjective interpretations of geostationary satellite data for nowcasting. *Nowcasting*. K. Browning, Ed., Academic Press, 149-166.

Rinehart, R. E., 2010: *Radar for Meteorologists, Fifth Edition*. Rinehart Publications, 482 pp.

Roberts, R. D., A. R. S. Anderson, E. Nelson, B. G. Brown, J. W. Wilson, M. Pocernich, and T. Saxen, 2012: Impacts of forecaster involvement on convective storm initiation and evolution nowcasting. *Wea. Forecasting*, **27**, 1061-1089.

Roberts, R. D., and S. Rutledge, 2002: Nowcasting storm initiation and growth using GOES-8 and WSR-88D data. *Wea. Forecasting*, **18**, 562-584.

Segal, M., and R. W. Arritt, 1992: Nonclassical Mesoscale circulations caused by surface sensible heat flux gradients. *Bull. Amer. Meteor Soc.,* **73**, 1593-1604.

Segal, M., W. E. Schreiber, G. Kallos, J. R. Garratt, A. Rodi, J. Weaver, and R. A. Pielke, 1989: The impact of crop areas in Northeast Colorado on midsummer mesoscale thermal circulations. *Mon. Wea. Rev.,* **117**, 809-825.

Sieglaff, J. M., L. M. Cronce, W. F. Feltz, K. M. Bedka, M. J. Pavolonis, and A. K. Heidinger, 2011: Nowcasting convective storm initiation using satellite-based box-averaged cloud-top cooling and cloud-type trends. *J. Appl. Meteor. Climatol.,* **50**, 110-126.

Soderholm, B., B. Ronalds, and D. J. Kirshbaum, 2014: The evolution of convective storms initiated by an isolated mountain ridge. *Mon. Wea. Rev.*, **142**, 1430-1451.

Stelten, S., and W. A. Gallus, 2017: Pristine Nocturnal Convective Initiation: A climatology and preliminary examination of predictability. *Wea. Forecasting*, **32**, 1613-1635.

Trier, S. B., J. W. Wilson, D. A. Ahijevych, and R. A. Sobash, 2017: Mesoscale vertical motions near nocturnal convection initiation in PECAN. *Mon. Wea. Rev.*, **145**, 2919-2941.

van den Heever, S. C., and Coauthors, 2021: The Colorado State University Convective CLoud Outflow and UpDrafts experiment (C^3LOUD-Ex). *Bull. Amer. Meteor. Soc.*, **102**, 1283-1305.

Weckwerth, T. M., 2000: The effect of small-scale moisture variability on thunderstorm initiation. *Mon. Wea. Rev.,* **128**, 4017-4030.

Weckwerth, T. M., and D. B. Parsons, 2006: A review of convection initiation and motivation for IHOP_2002. *Mon. Wea. Rev.*, **134**, 5-22.

Weckwerth, T. M., H.V. Murphey, C. Flamant, J. Goldstein, and C. R. Pettet, 2008: An observational study of convection initiation on 12 June 2002 during IHOP_2002. *Mon. Wea. Rev.*, **136**, 2283-2304.

Weckwerth, T. M., L. J. Bennett, L. J. Miller, J. V. Baelen, P. D. Girolamo, A. M. Blyth, and T. J. Hertneky, 2014: An observational and modeling study of the processes leading to deep, moist convection in complex terrain. *Mon. Wea. Rev.*, **142**, 2687-2708.

Wexler, A., 1976: Vapor pressure formulation for water in range 0 to 100 °C. – a revision. *Journal of Research of the National Bureau of Standards, Section A, Physics and Chemistry*. **80A**, 775-785.

Wilson, J. W., and R. D. Roberts, 2006: Summary of convective storm initiation and evolution during IHOP: observational and modeling perspective. *Mon. Wea. Rev.*, **134**, 23-47.

Wilson, J. W., and W. E. Schreiber, 1986: Initiation of convective storms at radar-observed boundary-layer convergence lines. *Mon. Wea. Rev.*, **114**, 2516-2536.

Wu C., B. Stevens, and A. Arakawa, 2009: What controls the transition from shallow to deep convection? *J. Atmos. Sci.*, **66**, 1793-1806.

Zhao, M., and P. H. Austin, 2005: Life cycle of numerically simulated shallow cumulus clouds: Part I: Transport. *J. Atmos. Sci.*, **62**, 1269-1290.

Zhu. P, 2015: On the mass-flux representation of vertical transport in moist convection. *J. Atmos. Sci.*, 72, 4445-4468.

Appendix A: Tables

Table 1: Specifications for UAS platforms and sensors deployed during LAPSE-RATE that contributed to this work (adapted from Barbieri et al. 2019). Nomenclature in table includes: CU-BST, University of Colorado-Boulder and Black Swift Technologies; UKY, University of Kentucky; UNL, University of Nebraska-Lincoln; OU, University of Oklahoma; FW, fixed-wing; R, multirotor; T, temperature; RH, relative humidity; P, pressure; MHP, multi-hole probe. Config. refers to the configuration of the temperature and humidity sensors: 3 – sensors have aspiration and solar shielding; 4 – sensors have solar shielding but no forced aspiration; 5 – sensors have aspiration but no solar shielding.

Operator	Platform (Type)	Config	Comp.	Model	Output	Accuracy
CU-BST	S1 (FW)	5	T, RH, P	Black Swift MHP	T: -40 to +85 °C RH: 0 to 100%	T: ± 0.3 °C RH: ± 3% RH P: ± 1.5 hPa
UKY	M600 (R)	3	T, RH, P	iMetXQ-2	T: -90 to +50 °C RH: 0 to 100% P: 10 to 1200 hPa	T: ± 0.3 °C RH: ± 5% RH P: ± 1.5 hPa Response times: T: 1 s @ 5 m s^{-1} RH: 0.6 s @ 25 °C P: 10 ms
UKY	SOLO (R)	3	T, RH, P	iMetXQ-2	See above	See above
UNL	M600 (R)	3	T, RH, P	iMetXQ-2	See above	See above
UKY	BLUECAT5 (FW)	3	T, RH, P	iMetXQ	T: -90 to +50 °C RH: 0 to 100% P: 10 to 1200 hPa	T: ± 0.3 °C RH: ± 5% RH P: ± 1.5 hPa Response times: T: 1 s @ 5 m s^{-1} RH: 0.6 s @ 25 °C P: 10 ms
UKY	S1000 (R)	3	T, RH, P	iMetXQ	See above	See above
OU	Coptersonde2 (R)	3	T	iMeT-XF PT100	T: -20 to +40 °C	± 0.3 °C Response time: 1 s
OU	Coptersonde2 (R)	4	RH	Innovative Sensor Technology HYT271	0 to 100%	± 1.8% RH Response time: 4 s
OU	Coptersonde2 (R)		P	TE Connectivity MS5611	10 to 1200 hPa	± 1.5 hPa Response time: 8 ms

Table 2: Data corrections applied to the UAS data based on the intercomparison results from Barbieri et al. 2019. A positive (negative) intercomparison mean difference implies a warm (cool) temperature bias, moist (dry) relative humidity bias, or high (low) pressure bias. The nomenclature and configurations follow that of Table 1.

Operator	Platform (Type)	Config.	Comp.	Intercomparison Mean Difference	Applied Correction
CU-BST	S1 (FW)	5	T	+1.19 °C	0
UKY	M600 (R)	3	T	+0.04 °C	-0.04 °C
UKY	SOLO (R)	3	T	-0.11 °C	+0.11 °C
UKY	BLUECAT5-B (FW)	3	T	+0.06 °C	+0.24 °C
UKY	BLUECAT5-D (FW)	3	T	+0.0157 °C	+0.484 °C
UKY	S1000 (R)	3	T	-0.23 °C	+0.23 °C
UNL	M600-1 (R)	3	T	-0.04 °C	+0.04 °C
UNL	M600-2 (R)	3	T	-0.08 °C	+0.08 °C
OU	Coptersonde2-A (R)	3	T	N/A	Corrected by OU
OU	Coptersonde2-B (R)	3	T	+0.12 to +0.38 °C	Corrected by OU
CU-BST	S1 (FW)	5	RH	-2.05 %	0
UKY	M600 (R)	3	RH	-5.45 %	+5.45%
UKY	SOLO (R)	3	RH	-5.97 %	+10.97 %
UKY	BLUECAT5-B (FW)	3	RH	-6.92 %	+6.92 %
UKY	BLUECAT5-D (FW)	3	RH	-6.26 %	+6.26%
UKY	S1000 (R)	3	RH	-7.60 %	+10.6 %
UNL	M600-1 (R)	3	RH	-1.53 %	+1.53 %
UNL	M600-2 (R)	3	RH	-2.74 %	+2.74 %
OU	Coptersonde2-A (R)	4	RH	N/A	Corrected by OU
OU	Coptersonde2-B (R)	4	RH	-9.54 to -0.53 %	Corrected by OU
CU-BST	S1 (FW)	5	P	+0.68 hPa	0
UKY	M600 (R)	3	P	+0.78 hPa	-0.78 hPa
UKY	SOLO (R)	3	P	+0.97 hPa	-0.97 hPa
UKY	BLUECAT5-B (FW)	3	P	+1.73 hPa	-1.73 hPa
UKY	BLUECAT5-D (FW)	3	P	+0.32 hPa	-0.32 hPa
UKY	S1000 (R)	3	P	+1.43 hPa	-1.43 hPa
UNL	M600-1 (R)	3	P	+0.61 hPa	-0.61 hPa
UNL	M600-2 (R)	3	P	+0.18 hPa	-0.18 hPa
OU	Coptersonde2-A (R)		P	+1.43 hPa	- 1.43 hPa
OU	Coptersonde2-B (R)		P	+1.83 hPa	- 1.83 hPa

Table 3: Information on surface-based sensors that contributed to this work (adapted from Hanft and Houston 2018). The nomenclature follows that of Table 1, with the addition of: FAA, Federal Aviation Administration; NWS, National Weather Service; MM, mobile mesonet; ASOS, automated surface observing system; AWOS, automated weather observing system; Td, dew point temperature; WS, wind speed; WD, wind direction.

Operator	Platform (Type)	Comp.	Model	Output	Accuracy
FAA	KRCV (AWOS)	T, Td, P, Wind		T: -128 to 54 °C Td: -62 to 30 °C P: 572 to 1067 hPa WS: 0 to 64 m s^{-1} WD: 0 to 360 °	T: ± 1 °C Td: ± 0.6 to 4.4 °C P: ± 0.7 hPa WS: ± 2 m s^{-1} or 5% WD: ± 5 °
FAA	K04V (AWOS)	T, Td, P, Wind		See above	See above
NWS	KALS (ASOS)	T, Td, P, Wind		T: -62 to 54 °C Td: -62 to 30 °C P: 572 to 1067 hPa WS: 0 to 64 m s^{-1} WD: 0 to 360 °	T: ± 0.6 to 4.4 °C Td: ± 0.6 to 4.4 °C P: ± 0.7 hPa WS: ± 2 m s^{-1} or 5% WD: ± 5 °
UNL	CoMeT (MM)	T (Slow), RH	Vaisala HMP155A-L-PT	T: -80 to +60 °C RH: 0 to 100%	T: ±(0.226 - 0.0028 × temperature) °C RH: ±(1.0 + 0.008 × reading) % Response time: 20 s
UNL	CoMeT (MM)	T (Fast)	Campbell Scientific 109SS-L Thermistor	-40 to +70 °C	± 0.1 °C Response time: 7.5 s (3 m s^{-1})
UNL	CoMeT (MM)	P	Vaisala PTB210	500-1100 hPa	± 0.25 hPa
UNL	CoMeT (MM)	Wind	RM Young 05103-L-PT	WS: 0 to 100 m s^{-1} WD: 0 to 360 °	WS: ± 1% WD: ± 3 °
UKY	Tower	T, RH	Campbell Scientific EE181-L	T: -40 to +60 °C RH: 0 to 100%	Temp: ± 0.2 °C RH: ±(1.3 + 0.003 × reading) %

Table 4: WSR-88D station altitude data for each of the three WSR-88D radars surrounding the SLV. KABX is the Alberqueque, NM radar, KGJX is the Grand Junction, CO radar, and KPUX is the Pueblo, CO radar.

Radar	Elevation (km MSL)	Tower Height (km AGL)	Radar Height (km MSL)
KABX	1.78918	0.01	1.79918
KGJX	3.04526	0.02	3.06526
KPUX	1.62458	0.01	1.63458

Table 5: Radar coverage information for the SLV. The beam heights were calculated using the Rinehart 2010 formula for both the nearest and furthest point of the SLV from each radar. The beam heights are provided in both kilometers above MSL and kilometers AGL, using the average elevation of the SLV as the ground level. KABX is the Alberqueque, NM radar, KGJX is the Grand Junction, CO radar, and KPUX is the Pueblo, CO radar.

Radar	Elevation Angle	Distance to Nearest Point of SLV (km)	Height of Beam Center at Nearest Point of SLV (km MSL / km AGL)	Distance to Furthest Point of SLV (km)	Height of Beam Center at Furthest Point of SLV (km MSL / km AGL)
KABX	0.5°	264	N/A (Beam Blocked)	340	N/A (Beam Blocked)
KABX	1.5°	264	13.0 / 10.7	340	17.5 / 15.2
KGJX	0.5°	205	N/A (Beam Blocked)	277	N/A (Beam Blocked)
KGJX	1.5°	205	10.9 / 8.6	277	14.8 / 12.5
KPUX	0.5°	148	4.2 / 1.9	210	6.1 / 3.8
KPUX	0.9°	148	5.2 / 2.9	210	7.5 / 5.2
KPUX	1.3°	148	6.3 / 4.0	210	9.0 / 6.7
KPUX	1.8°	148	7.6 / 5.3	210	10.8 / 8.5

Table 6: Convective parameter mean values from UAS-modified soundings from 1700-1830 UTC for each land-use region. The 100-mb mixed layer parcel was used. There were 15 modified soundings from the NIrgR and 13 from the IrgR. The probability value was determined using a two-tailed t-test. A probability value less than 0.05 indicates the difference between the two regions was statistically significant.

Convective Parameter	1729 UTC Moffat	NIrgR Mean (n=15)	IrgR Mean (n=13)	Probability Value (*p*)
CAPE (J kg^{-1})	281.31	365.38	274.80	0.14286
CIN (J kg^{-1})	-54.33	-28.91	-58.59	0.00171
ACBLLR (K km^{-1})	8.384	8.285	8.194	0.46366
Δz^* (m)	492	492	492	N/A
LCL Pressure (hPa)	622.28	609.62	620.46	0.01264
LCL Height (m AGL)	1811	2011	1906	0.04925
LFC Pressure (hPa)	588.10	588.15	584.90	0.38590
LFC Height (m AGL)	2342	2303	2388	0.11704

Table 7: Convective parameter mean values from surface-modified soundings from 1700-1830 UTC for each land-use region. The surface-based parcel was used. There were 24 modified soundings from the NIrgR and 13 from the IrgR. The probability value was determined using a two-tailed t-test. A probability value less than 0.05 indicates the difference between the two regions was statistically significant.

Convective Parameter	**1729 UTC Moffat**	**NIrgR Mean (n=24)**	**IrgR Mean (n=13)**	**Probability Value (*p*)**
CAPE (J kg^{-1})	628.52	1051.93	1194.28	0.258898
CIN (J kg^{-1})	0	-6.32	-2.24	0.450182
ACBLLR (K km^{-1})	8.1059	8.6795	8.7282	0.689955
Δz^* (m)	492	492	492	N/A
LCL Pressure (hPa)	605.38	615.54	628.99	0.012696
LCL Height (m AGL)	2107	1919	1789	0.048290
LFC Pressure (hPa)	592.01	597.82	611.25	0.001977
LFC Height (m AGL)	2288	2157	2025	0.007680

Appendix B: Figures

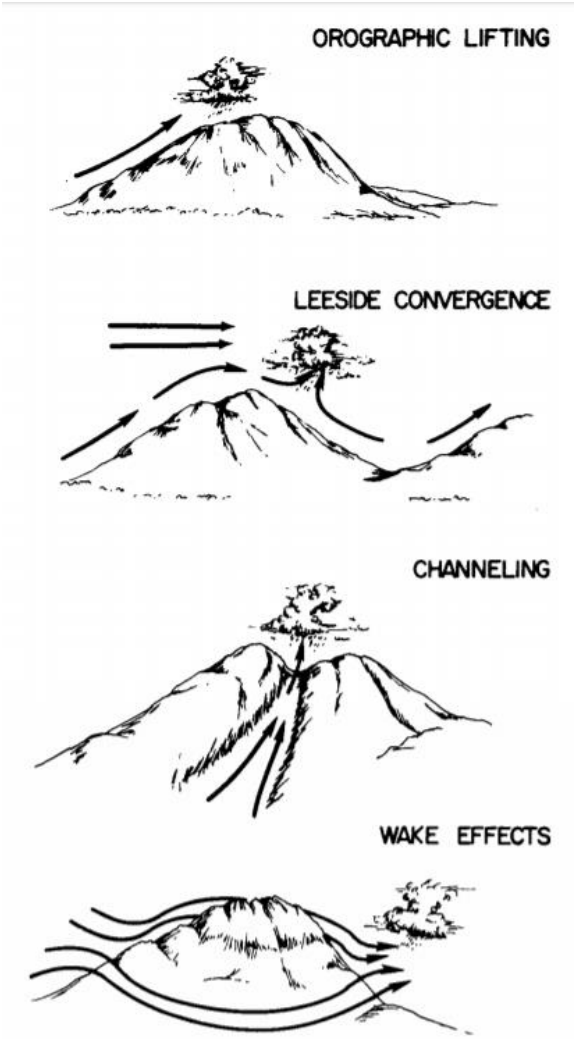

Figure 1: Orographic convergence mechanisms that can lead to DCI, from Banta and Barker Schaaf 1987.

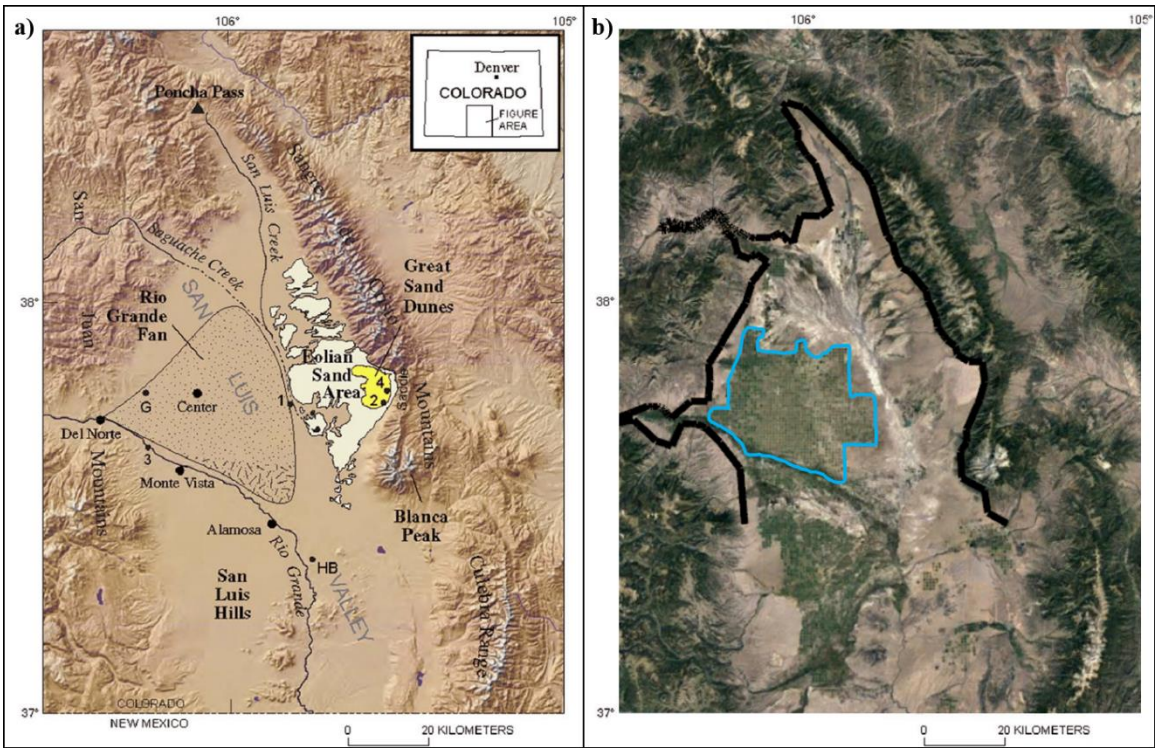

Figure 2: a) A map of the SLV with labeled geographic features, taken from Madole et al. 2008. The map base is from the U.S. Geological Survey color shaded-relief map of Colorado. b) The same region as panel A, but as visible imagery taken from Google Earth, illustrating the land-use differences within the SLV. The SLV is outlined in black on Panel B, and the approximate location of the irrigated region is outlined in light blue.

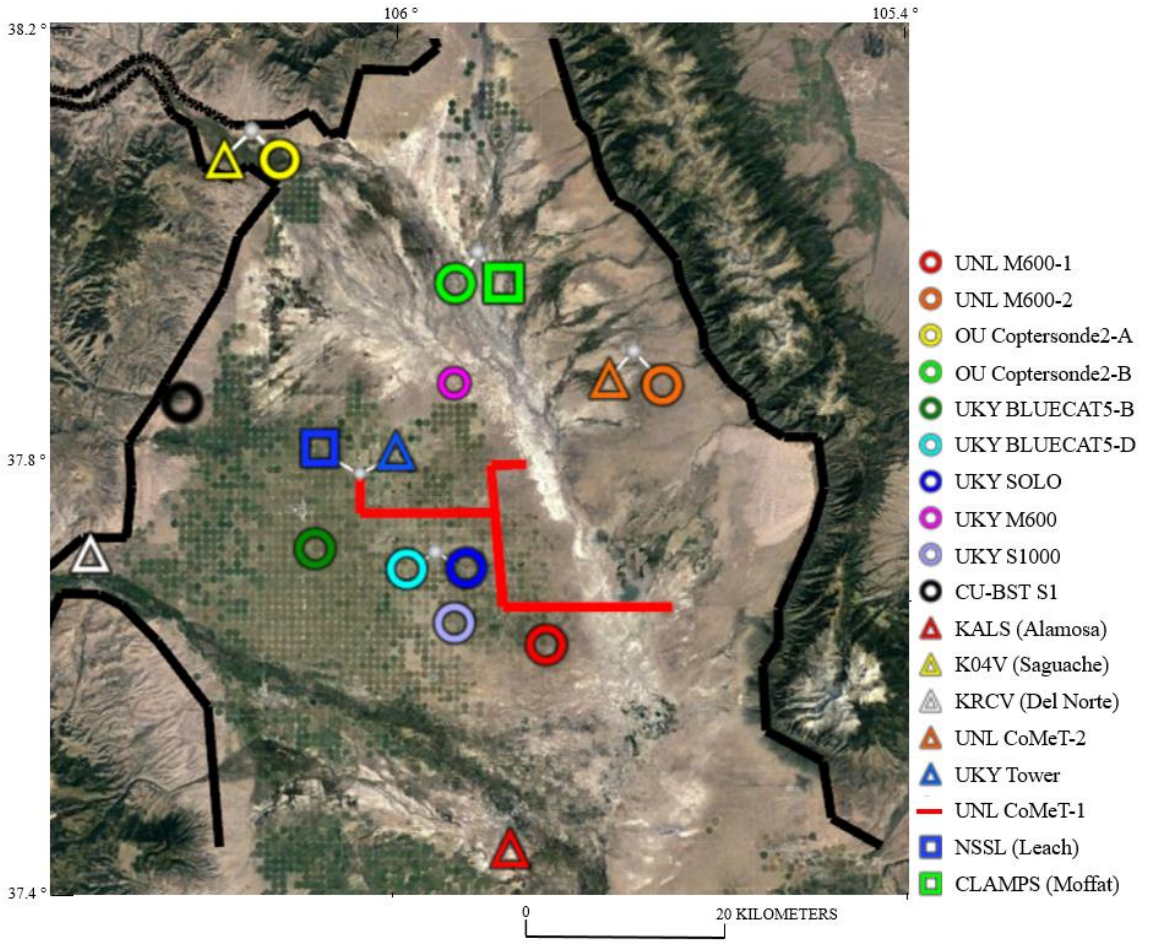

Figure 3: The locations of instruments in the SLV during LAPSE-RATE IOP1. Circles represent UAS, triangles represent surface-based observing systems, and squares represent radiosonde launch locations. The symbols of collocated instruments were offset from their exact location for clarity (e.g. OU Coptersonde2-A and K04V). The red line represents a mobile mesonet transect path. The nomenclature used in the legend follows that of Tables 1 and 2, with the addition of: NSSL, National Severe Storms Laboratory; CLAMPS, Collaborative Lower Atmospheric Profiling System. The SLV is outlined in black.

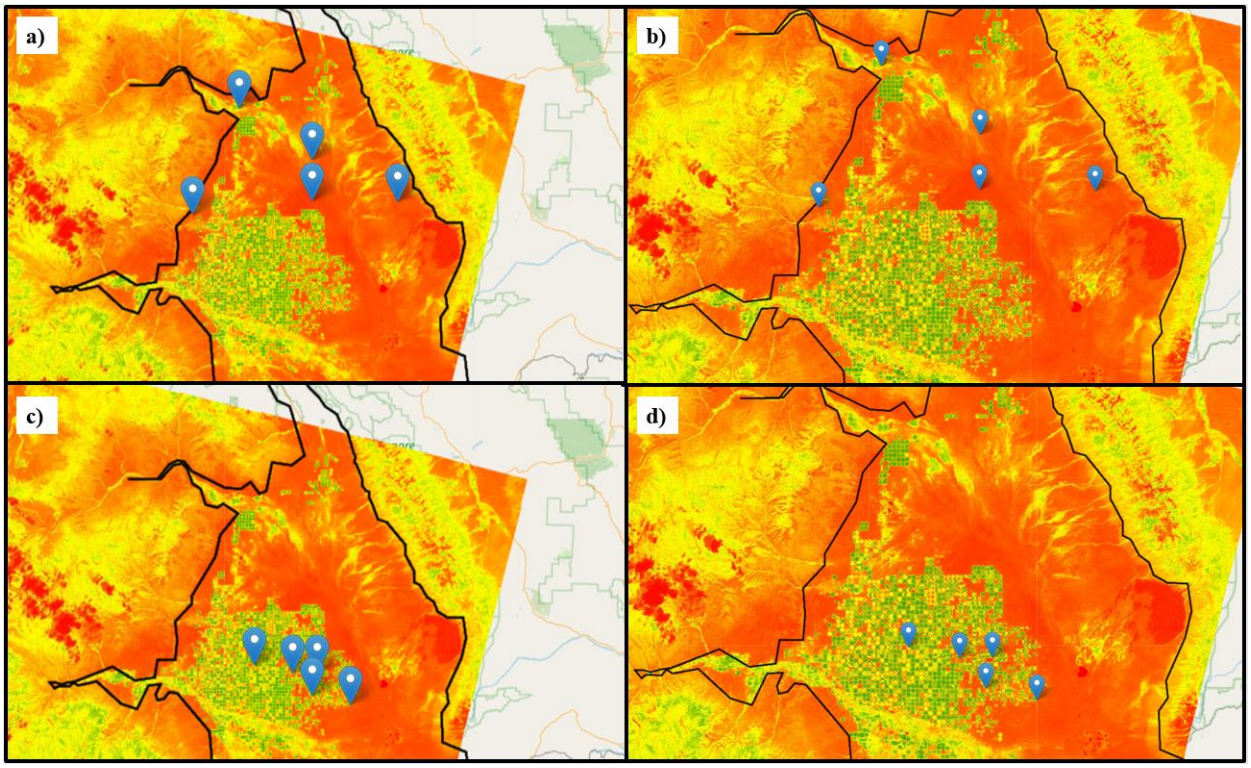

Figure 4: LANDSAT-8 Normalized Difference Vegetation Index (NDVI) imagery of the SLV from June 2018. NDVI is a measure of plant photosynthetic activity. Green indicates more photosynthetic activity, red indicates less. The blue icons represent UAS profiling locations. a) shows the location of UAS classified as non-irrigated sites from a localized perspective. b) is the same as a), but with a localized perspective that views the entire SLV. c) and d) are the same as a) and b), respectively, but the icons represent UAS classified as irrigated sites. The SLV is outlined in black.

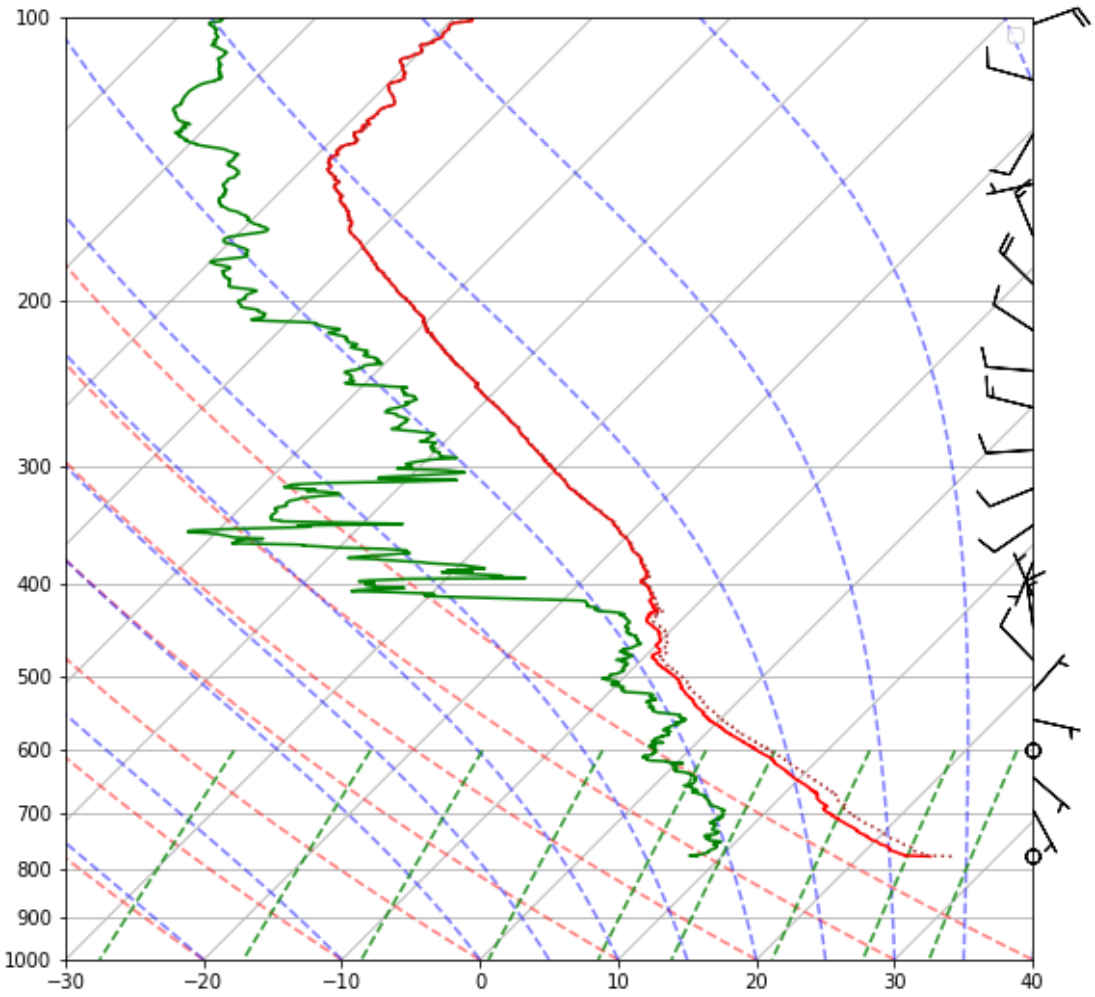

Figure 5: Environmental profile sampled by a radiosonde launched by CLAMPS in Moffat, Colorado, at 1729 UTC during IOP1. The solid red line represents the environmental temperature, the solid green line the environmental dew point temperature, and the dotted brown line the environmental virtual temperature.

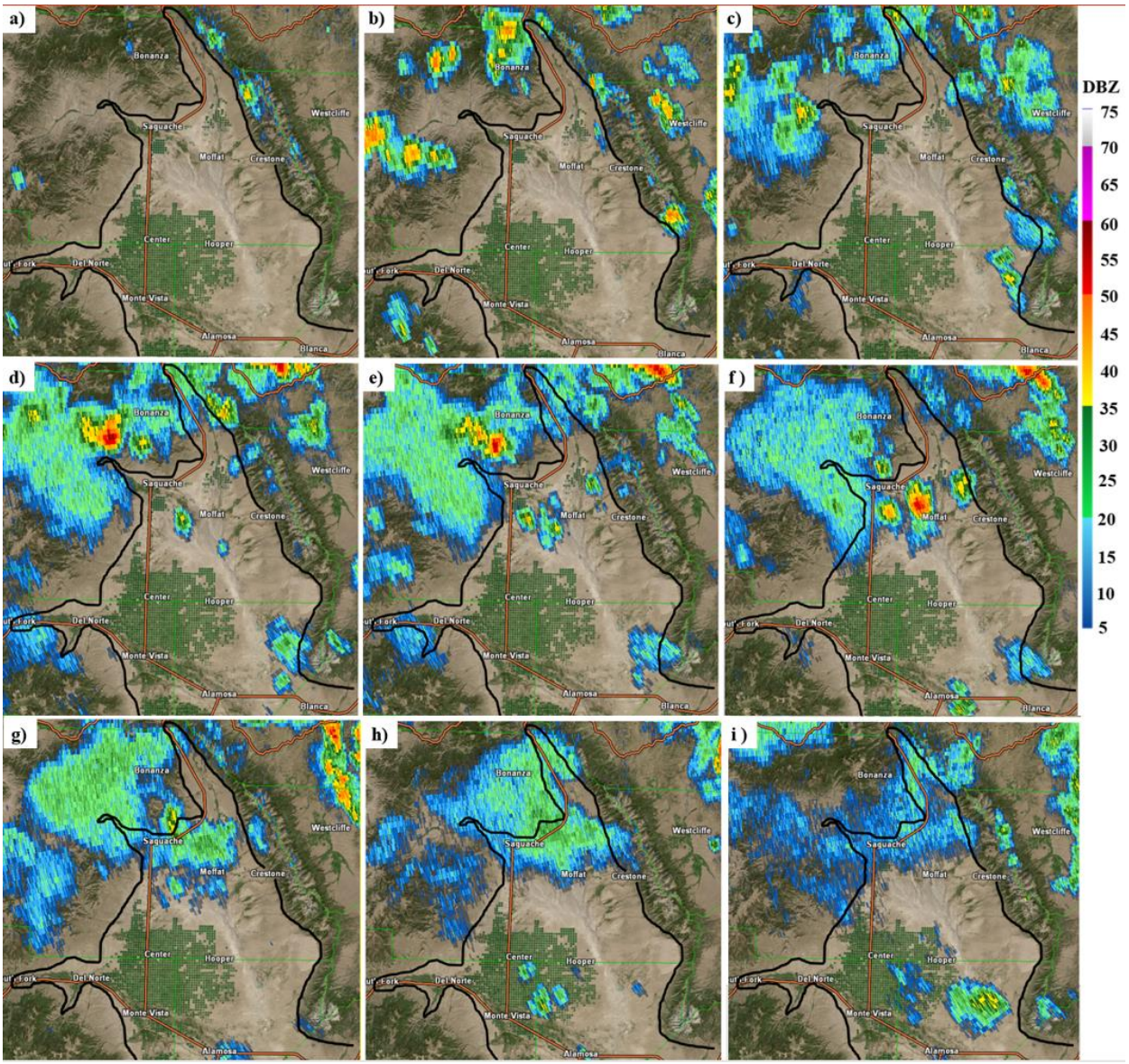

Figure 6: Key times in the KPUX (Pueblo, CO) radar evolution over the SLV during IOP1. a) is the 0.5° scan at 1655 UTC, b) is the 0.5° scan at 1801 UTC, c) is the 1.3° scan at 1845 UTC, d) is the 0.9° scan at 1917 UTC, e) is the 0.9° scan at 1933 UTC, f) is the 1.3° scan at 1950 UTC, g) is the 0.5° scan at 2035 UTC, h) is the 0.9° scan at 2126 UTC, and i) is the 0.9° scan at 2215 UTC. The SLV is outlined in black.

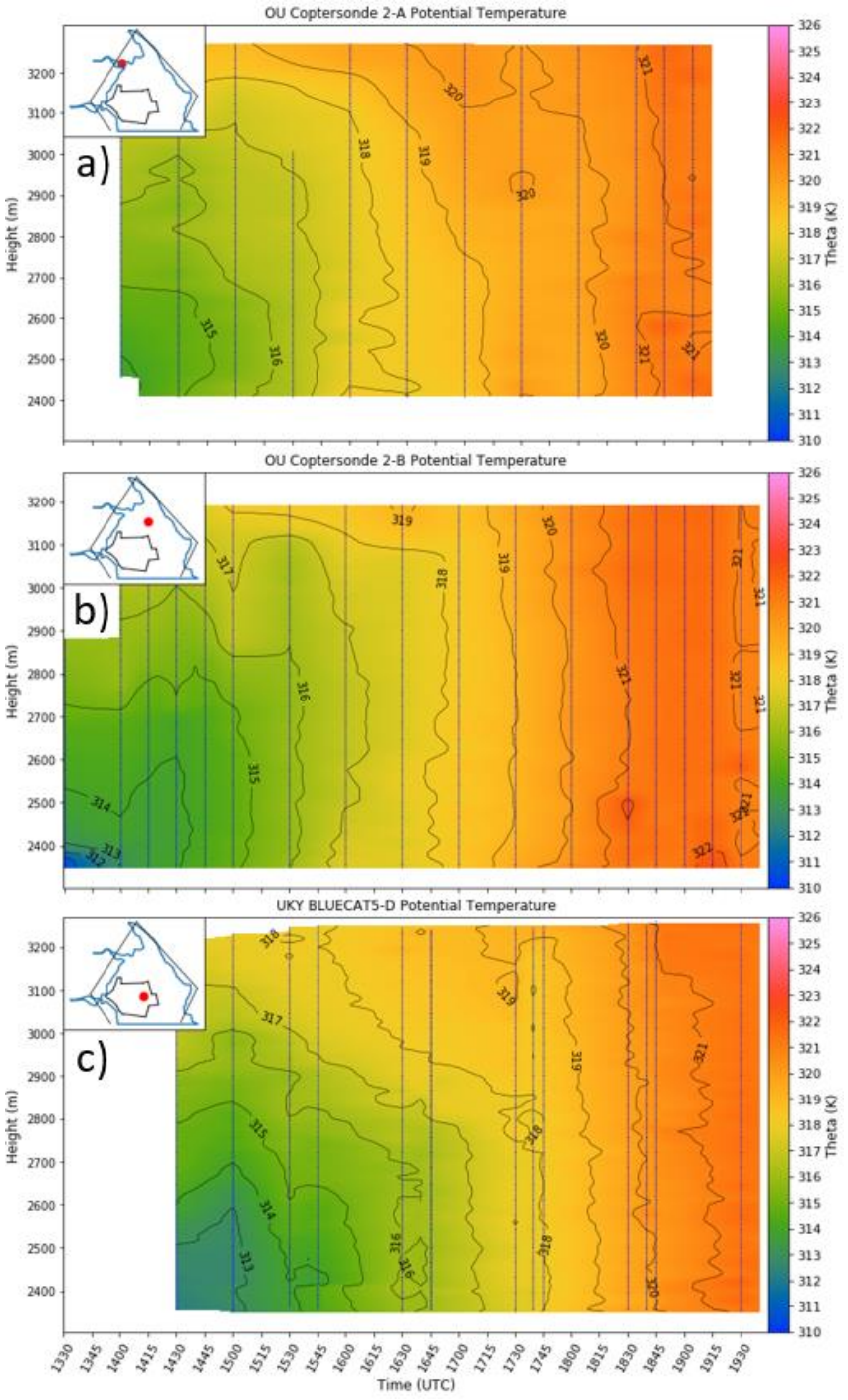

Figure 7: Time-height vertical cross sections of potential temperature during IOP1 for a) OU Coptersonde 2-A, b) OU Coptersonde 2-B, and c) UKY BLUECAT 5-D. Vertical blue lines indicate the flight times. The inset map shows the sampling location (red dot) within the SLV. The innermost black contour on the inset map outlines the approximate boundary of the irrigated region, the blue line indicates the edge of the valley (south of Alamosa, Colorado, not shown), and the outermost black line the approximate location of the mountain crests.

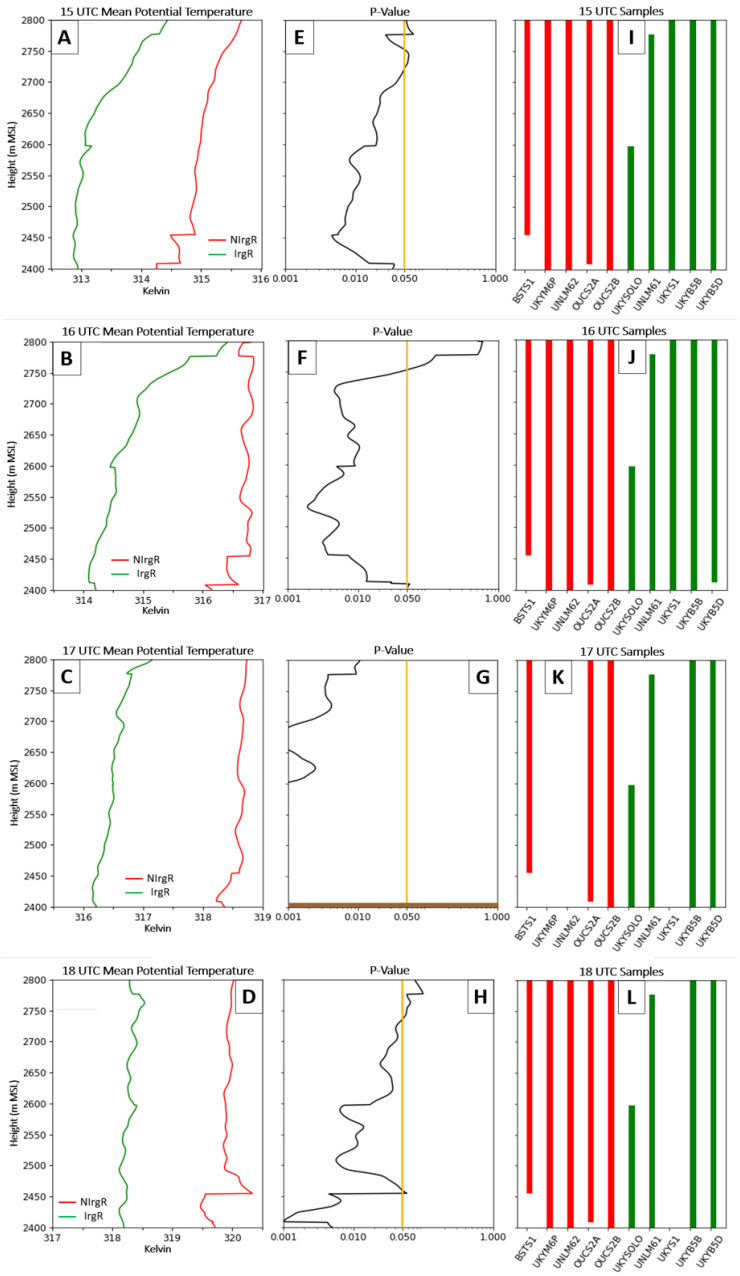

Fig. 8: Results of two-sided t-test on potential temperature at height levels between 2400-2800 meters above MSL. The rows from top to bottom are 15, 16, 17, and 18 UTC. The left column (a-d) displays mean values with height, with the NIrgR in red and the IrgR in green. The middle column (e-h) displays the p-value with height. The vertical yellow line represents p = 0.05. Values to the left of the yellow line are statistically significant at the 95% confidence level. The brown shading in Panel B represents levels at which the p-value could not be calculated. The right column (i-l) displays the heights at which data was available from each UAS. NIrgR sites are plotted in red, IrgR sites are plotted in green. The UAS nomenclature used in the right column is an abbreviated form of the platform names used in Fig. 3.

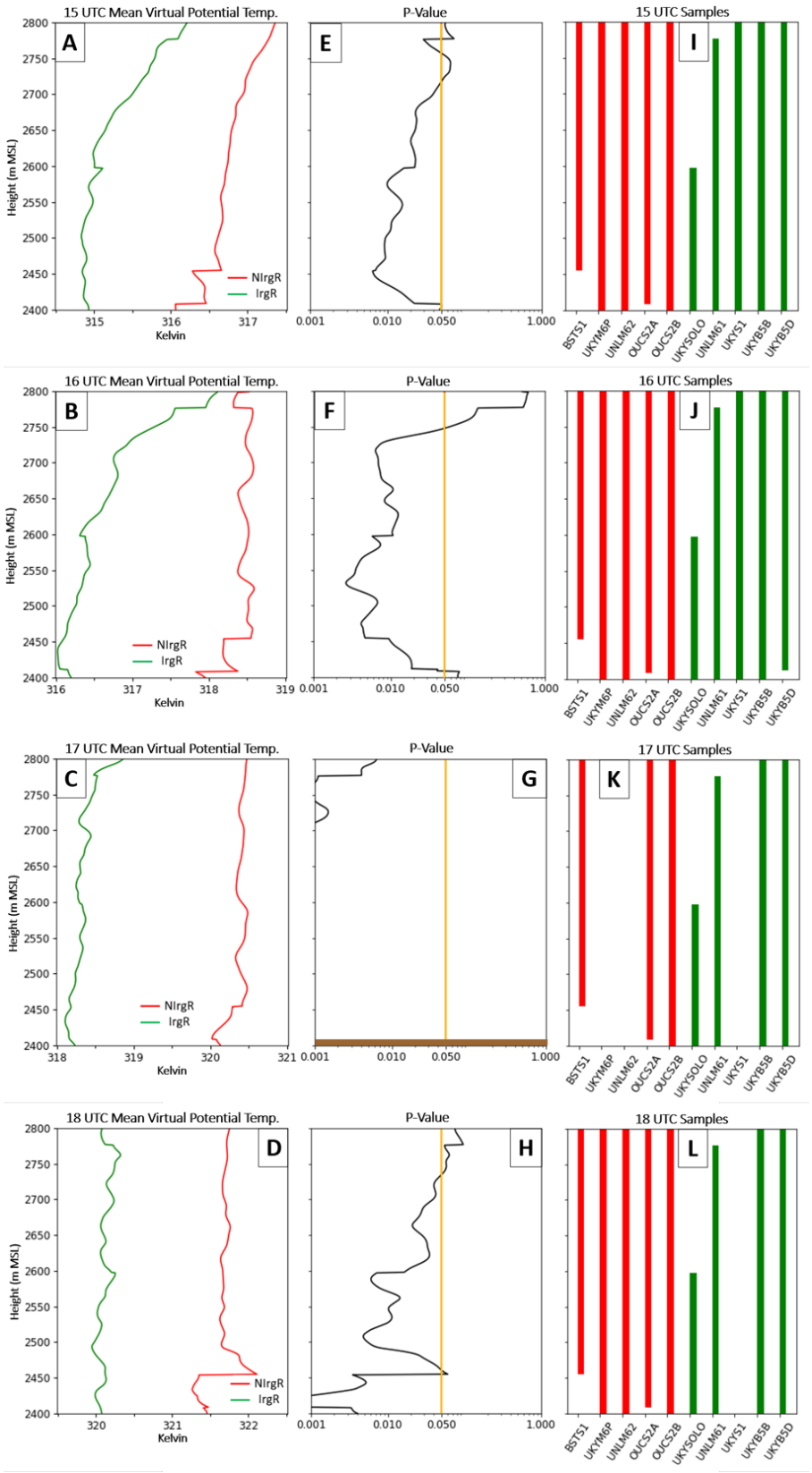

Fig. 9: The same as Fig. 8, but for virtual potential temperature.

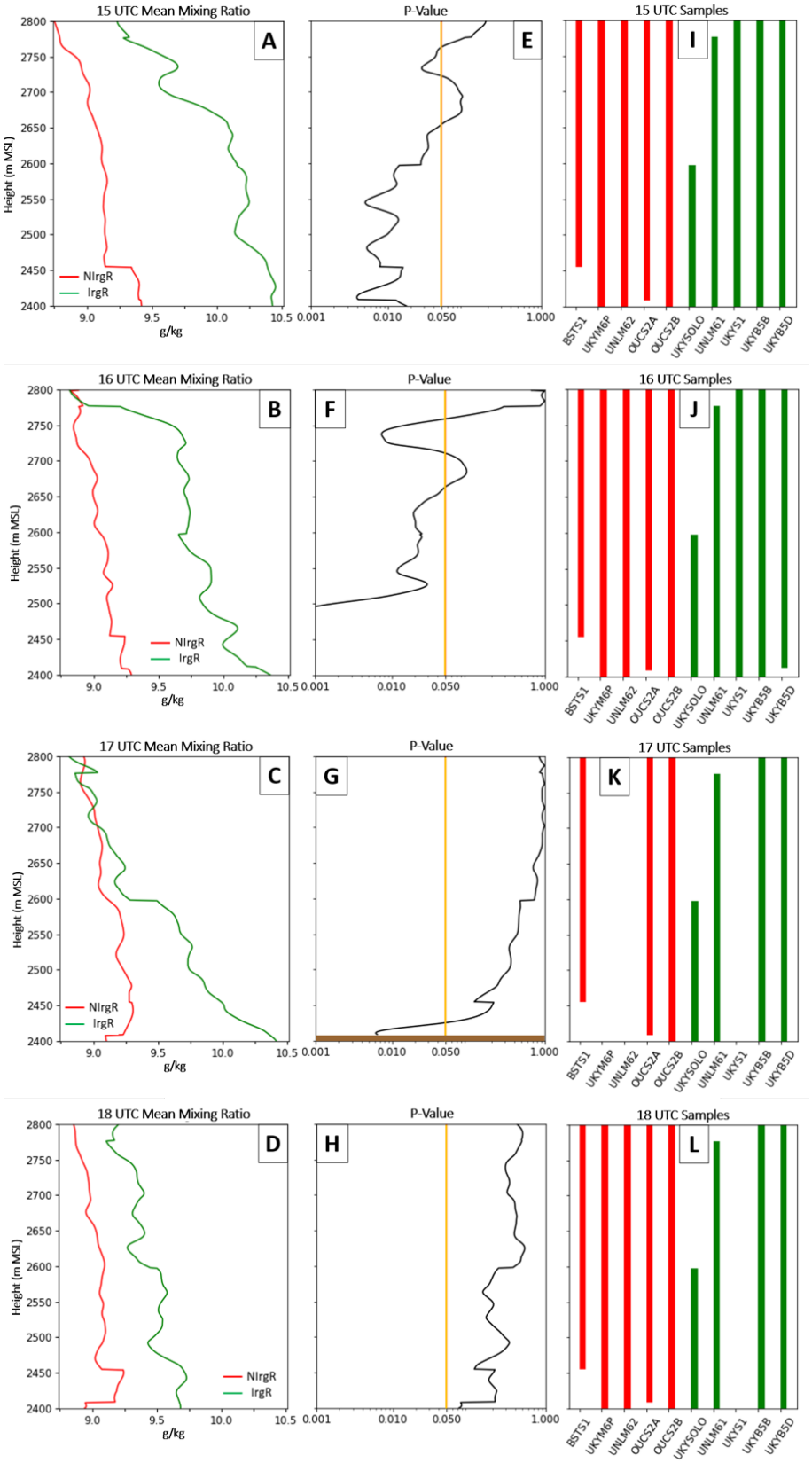

Fig. 10: The same as Fig. 8, but for mixing ratio.

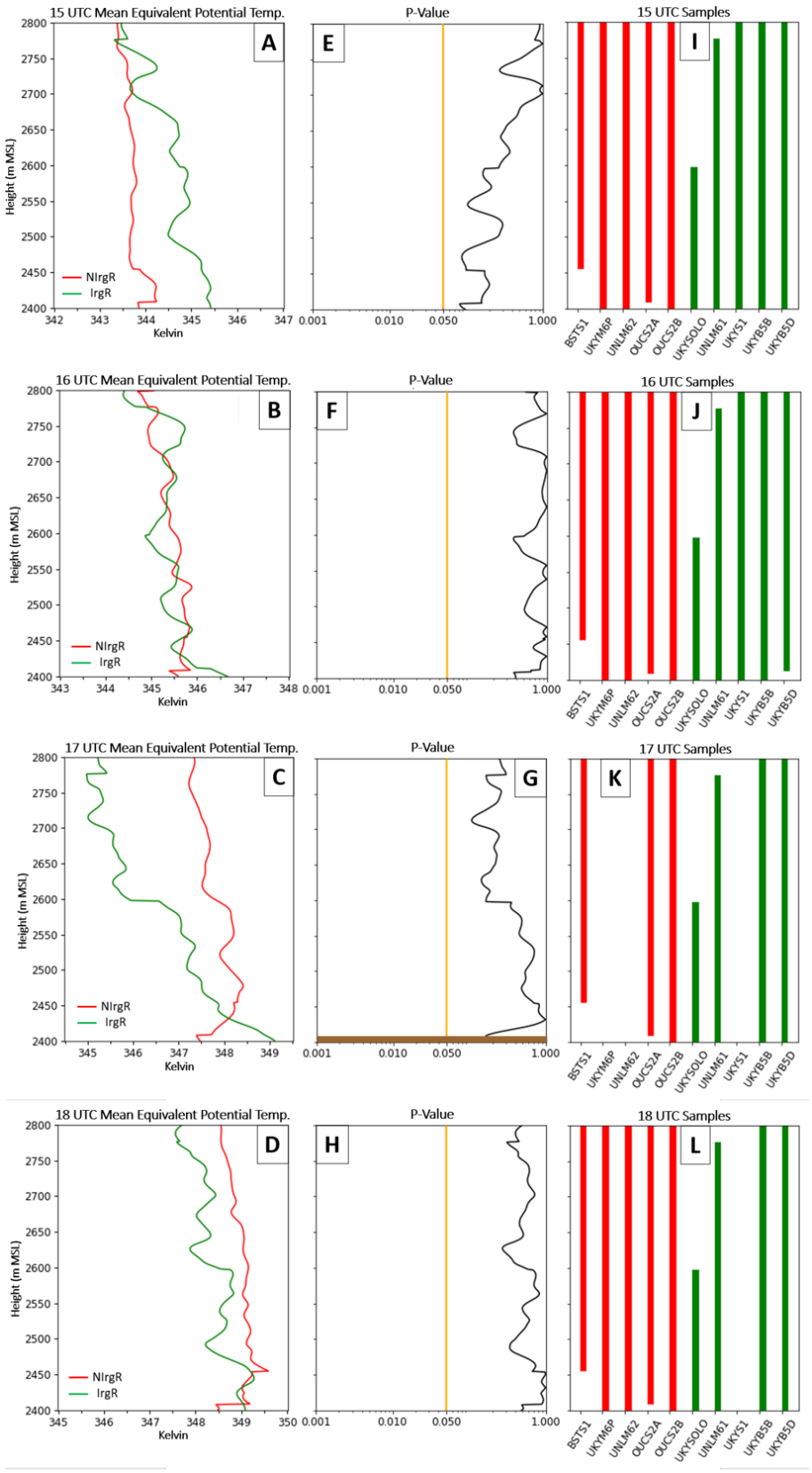

Fig. 11: The same as Fig. 8, but for equivalent potential temperature.

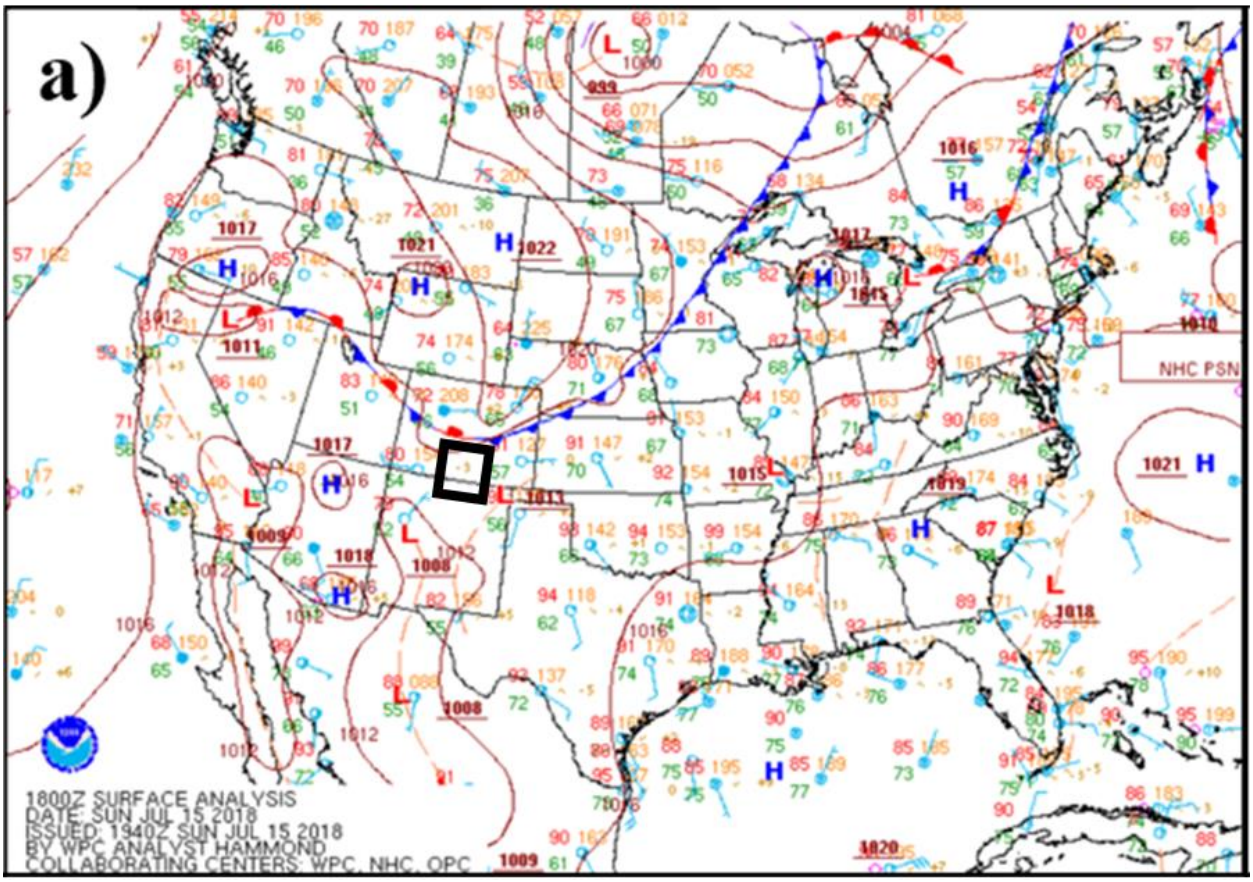

Figure 12: 18 UTC surface analysis from the NOAA Weather Prediction Center illustrating a cold front extending southeastward from Minnesota across the central Plains into central Colorado. The black box over southern Colorado indicates the location of the SLV.

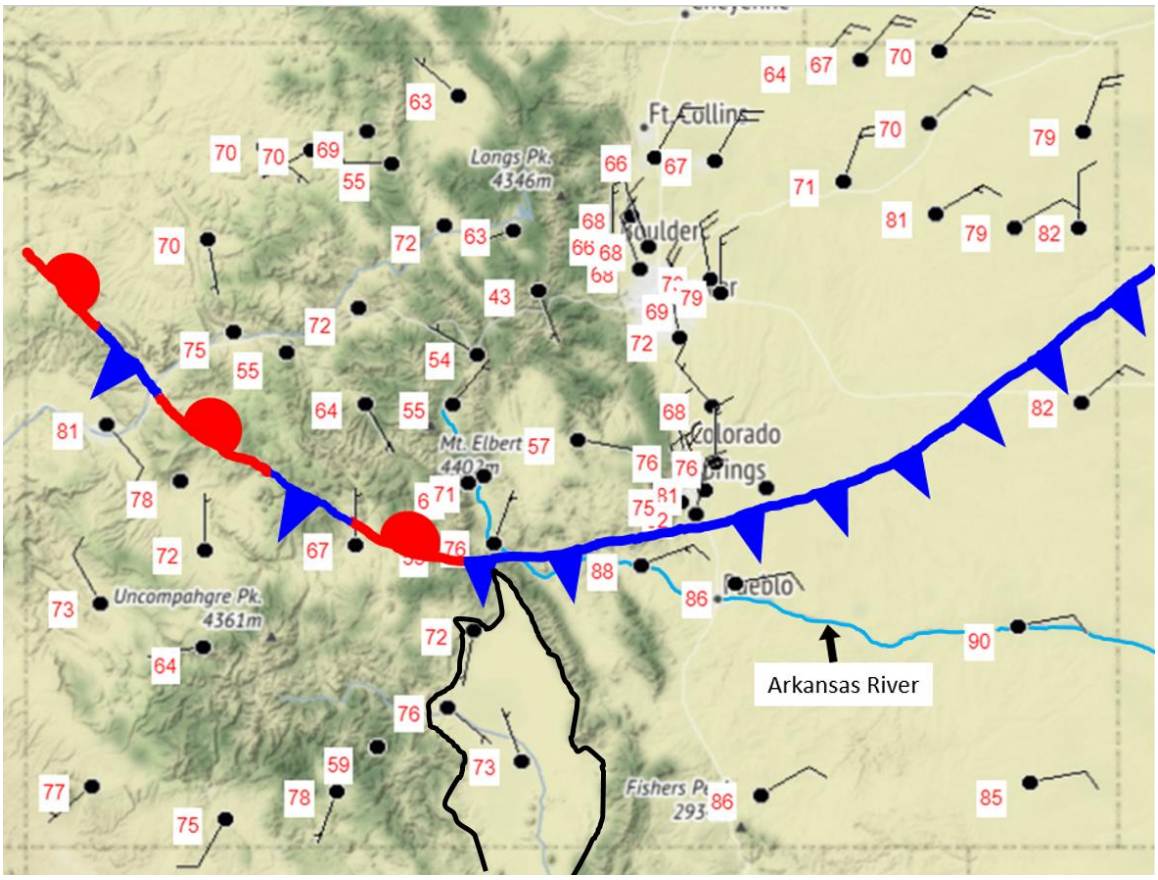

Figure 13: 17 UTC surface temperature (red numbers) and wind barbs from ASOS/AWOS stations across Colorado. Map generated using MesoWest. The SLV is outlined in black. The frontal boundary was annotated.

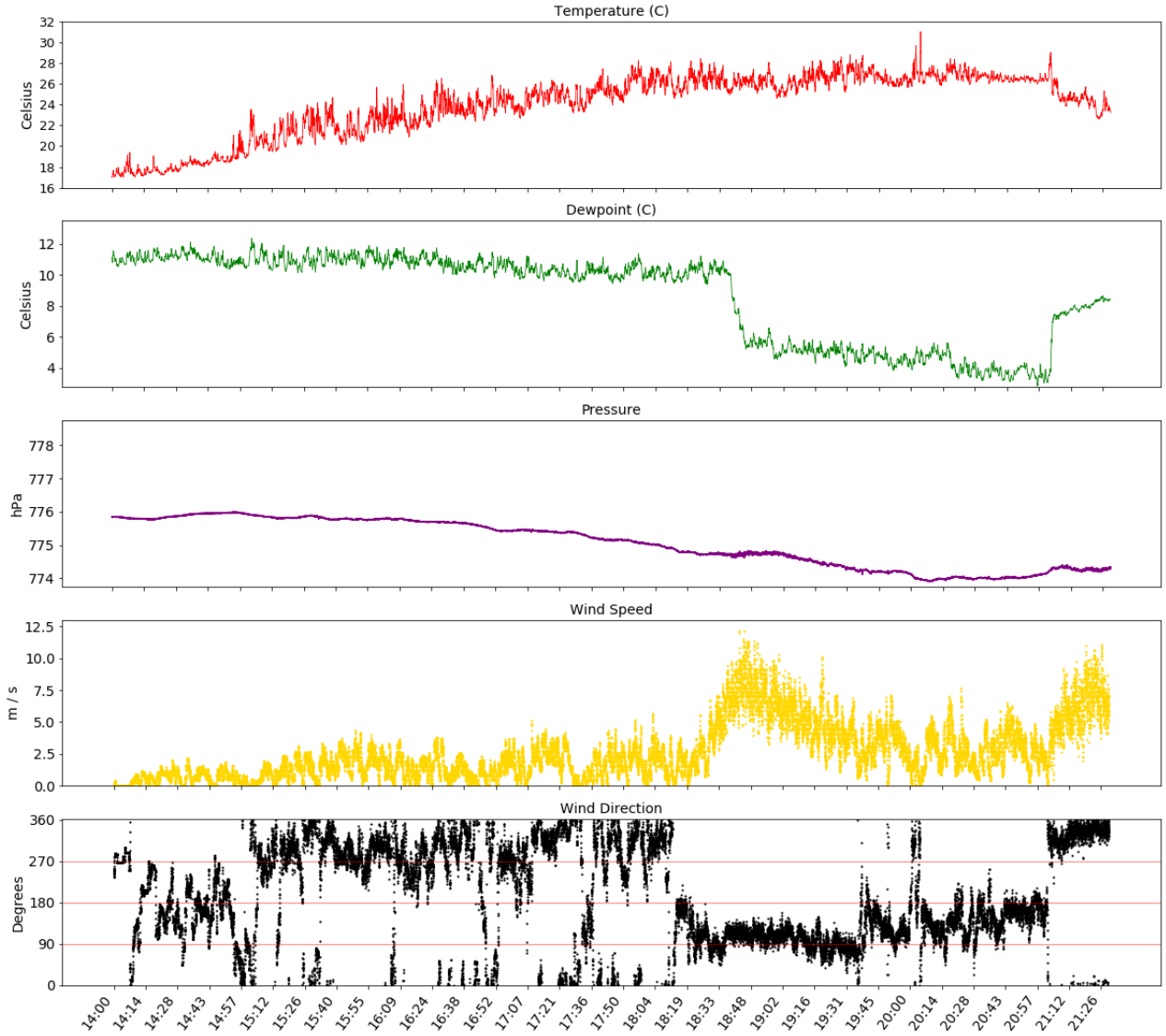

Figure 14: Meteogram of CoMeT-2 observations between 1400-2130 UTC. The rows, from top to bottom, are: temperature (red), dew point temperature (green), pressure (purple), wind speed (yellow), wind direction (black). The horizontal red lines on the wind direction plot indicate west (270°), south (180°), and east (90°). The times listed along the x-axis are HH:MM UTC.

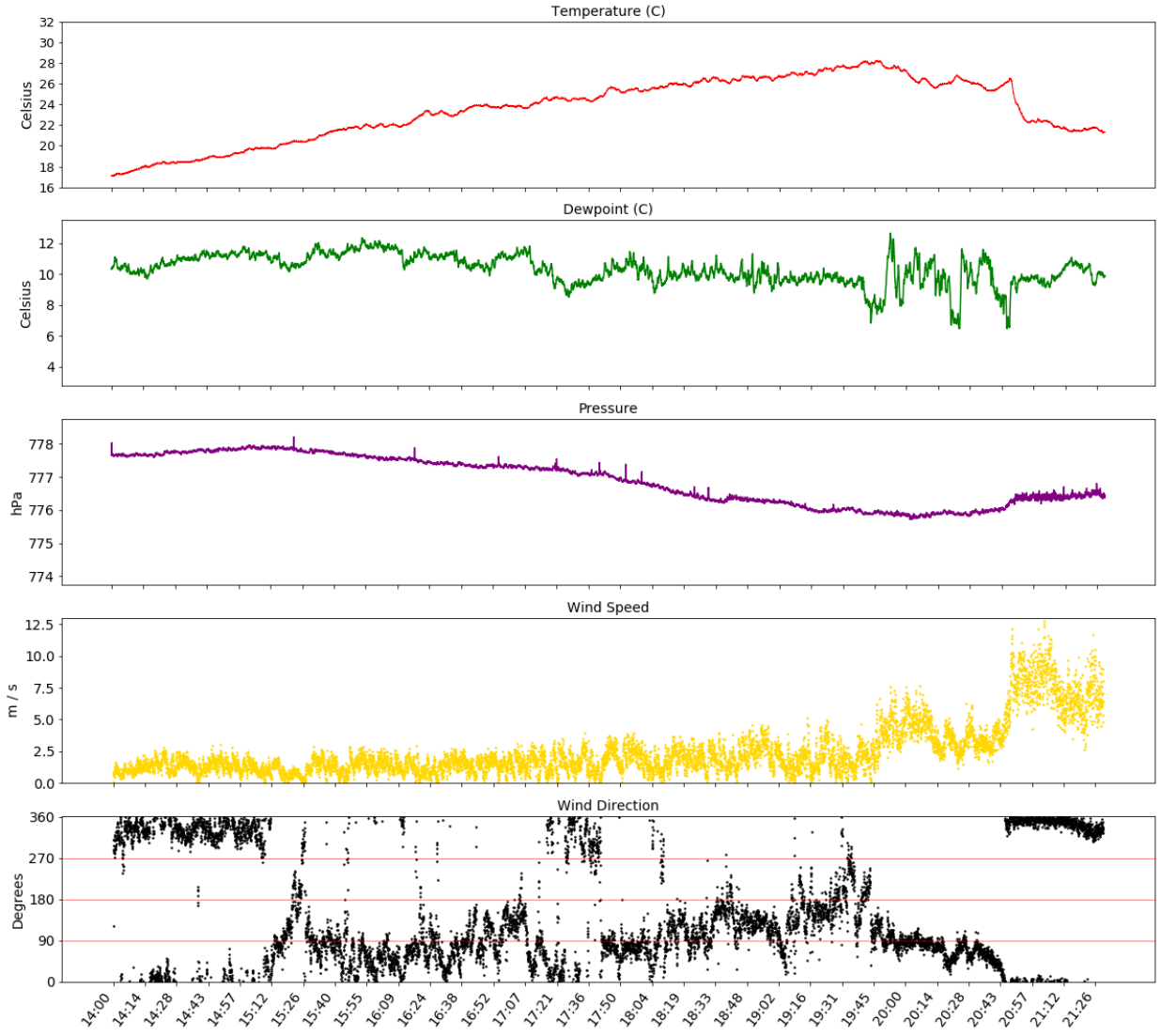

Figure 15: Meteogram of UKY Tower observations between 1400-2130 UTC, following the same plot format as Figure 26.

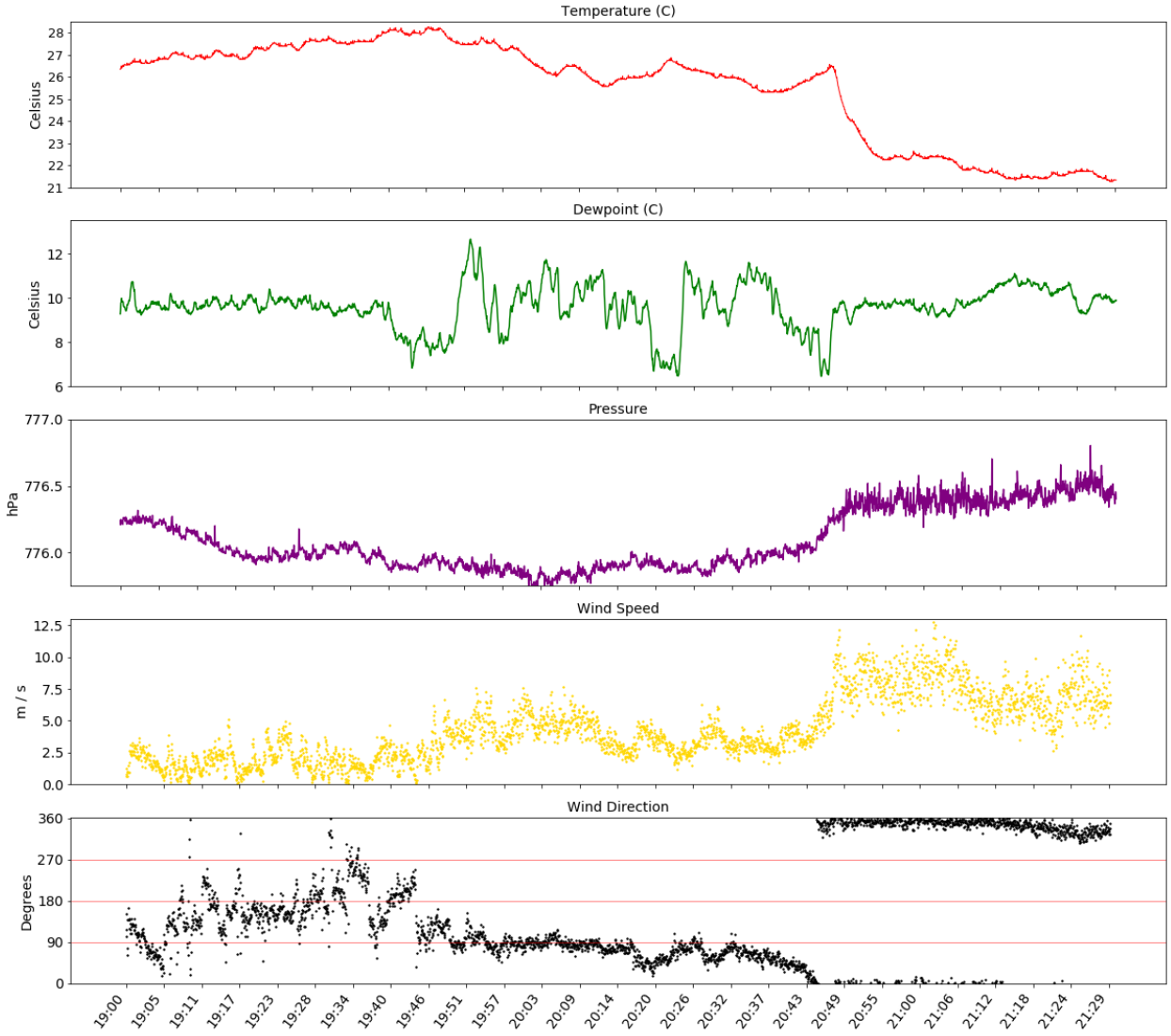

Figure 16: Meteogram of UKY Tower observations between 1900-2130 UTC, following the same plot format as Figure 26.

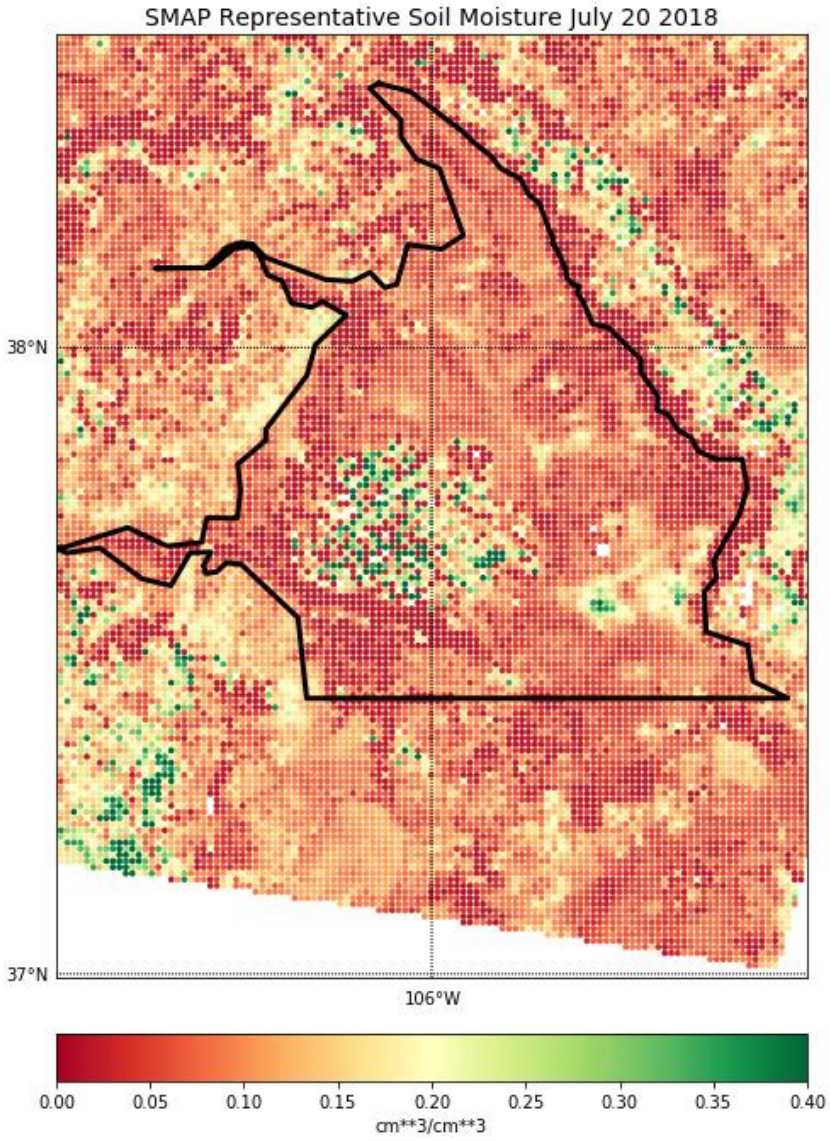

Figure 29: Soil Moisture Active Passive (SMAP) data from the National Snow and Ice Data Center for the SLV and surrounding areas on 20 July 2018. Warmer colors indicate lower soil moisture values. The SLV is outlined in black.